Forecasting Research

Met O 11 Scientific Note No 3

A geometric model of balanced, axisymmetric flows with embedded penetrative convection

by

G.J. Shutts, M. Booth and J. Norbury

February 1988

orological Office (Met O 11)
racknell, Berkshire RG12 2SZ, England

MET O 11 SCIENTIFIC NOTE NO 3

A GEOMETRIC MODEL OF BALANCED, AXISYMMETRIC FLOWS WITH EMBEDDED PENETRATIVE CONVECTION.

by

G.J. Shutts, M. Booth and J. Norbury.

FEBRUARY 1988.

Met O 11 (Forecasting Research)
Meteorological Office
London Road
Bracknell Berkshire RG12 2SZ
ENGLAND.

Abstract

A Lagrangian element model is described which represents axisymmetric flow as a set of toroidal elements, each of which is homogeneous in potential temperature and angular momentum. The flow is assumed to be in gradient wind and hydrostatic balance at all times; this requires that all element interfaces satisfy the rotational equivalent of Margules' formula for the slope of a front. For the flow to be convectively and inertially stable, the element geometry can be shown to adopt a unique configuration at any time. This may be precisely expressed as a requirement for a modified pressure function to be convex in a certain mapping of the space co-ordinates.

Impulses of heat are offered to groups of elements so as to simulate the release of latent heat energy during moist convection. The subsequent element configuration represents the balanced equilibrium state resulting from penetrative convection when the azimuthal-mean angular momentum is conserved. The model demonstrates the formation of a low-level warm core cyclone bounded by a frontal surface and an upper-level anticyclonic lens composed of convected elements. It provides a simple picture of the role of convection in explosive cyclogenesis, polar low and hurricane formation and allows some aspects of the co-operative interaction between synoptic and convective scale to be treated explicitly - without parametrization.

1. Introduction

A novel, geometric interpretation and extension of semi-geostrophic theory was recently put forward by Cullen and Purser (1984). The idea behind their technique can be traced back to the graphical solution procedure used by Hoskins and Bretherton (1972) to solve the zero potential vorticity, deformation - forced frontal problem. In this special case, potential temperature (θ) and absolute momentum (M_g) surfaces coincide and their slope is proportional to $dM_g/d\theta$. Since M_g (but not θ) evolves in time as deformation is imposed, the slope of these straight line contours changes and contours may collide at a boundary forming a front. Instead of regarding these lines as contours of M_g and θ in the continuous problem, Cullen (1983) solved the same problem with a finite number of elements - each being uniform in M_g and θ. He showed how this graphical method could be extended to find solutions after the point when a discontinuity forms in the continuous problem, implying the growth of a true discontinuous front into the interior of the fluid.

Cullen and Purser (1984) then showed how the method could be extended to a system in which elements of the same θ value could have different M_g values thereby providing a finite representation of the non-zero potential vorticity problem. The key to this extension was the identification of a certain pressure function which must be convex for convective and inertial stability. The graphical solution approach then becomes equivalent to the geometrical construction of a multi-facetted convex shell defined by the intersection of a set of planes whose slopes are given by the M_g and θ

values of the corresponding elements (Cullen et al, 1987). The generalization to three-dimensional flows, where elements are convex polyhedra, is straightforward in principle.

Shutts (1987) gave an example of how 'Geometric' models can automatically describe a form of penetrative convection involving no entrainment. The model only recognises balanced equilibrium states after the mass transferred by convection has completed an inviscid geostrophic adjustment: the details of the unbalanced flow associated with the convection itself are not described. The principal feature of these balanced flow 'after-states' in the Geometric model is the creation of a mesoscale lens out of fluid which has convected, and a front in the region from which the fluid was drawn. Analytic models of this process for rectilinear flow are described in Shutts (1987).

The treatment of convection as an agency for mass transfer was also considered by Gill et al (1979) and Smith (1981). Both found the balanced axisymmetric flow states of one layer or multi-layer homogeneous fluids resulting from mass removal or redistribution. To some extent their results anticipate the discontinuous flow structures predicted here. Other studies using balanced, axisymmetric models have tended to concentrate on the toroidal circulations and flow evolution resulting from heat or momentum forcing in vortices with differing inertial stability and baroclinity (eg Shapiro and Willoughby, 1982; Schubert and Hack, 1982; Schubert and Hack, 1983). For the most part, these studies were directed at tropical cyclones yet there is growing evidence of a variety of mesoscale vortices to which this work is relevant.

The problem of how convection interacts with its synoptic and mesoscale environment is one of the great challenges of dynamical meteorology today. Evidence exists to suggest that the role of the moist process in extratropical weather systems is more profound than a simple modification to the effective static stability experienced by air parcels. Depressions containing active convection often exhibit explosive growth (Reed and Albright, 1986) and frequently take on a hurricane-like appearance with the formation of a cloud-free 'eye' of the storm. 'Polar low' vortices are another example of a weather system in which convection plays a major part in determining the structure and evolution of the wind and temperature field (Rasmussen, 1985). In both Reed and Albright's and Rasmussen's studies, the onset of intense convection appears to have been associated with the formation of a low-level warm-cored cyclonic vortex.

In this paper we will describe an extension of the Geometric model to the axisymmetric case where M_g is replaced by the gradient wind angular momentum, M. Idealized convection experiments are presented in which an annular region of a rotating, stratified fluid is given a heat impulse so that it convects to the upper part of the model atmosphere. The resulting balanced states will be discussed with respect to observational studies of polar lows and explosive cyclogenesis.

2. The Axisymmetric, Geometric Model: Theoretical basis

(a) Convexity principle

A symmetrically stable, balanced vortex was shown by Fjortoft (1946) and Eliassen and Kleinschmidt (1957) to be a minimum energy state with respect to toroidal parcel displacements which conserve potential temperture and angular momentum. The extremum in energy corresponds to the gradient wind and hydrostatic requirements:

$$\frac{v^2}{r} + 2\Omega v = \frac{\partial \phi}{\partial r} \qquad (1)$$

and

$$g \frac{\theta}{\theta_o} = \frac{\partial \phi}{\partial z} \qquad (2)$$

respectively, where v is the tangential velocity, r is the radius, z is the pseudo-height of Hoskins and Bretherton (1972), ϕ is the geopotential, θ is the potential temperature with constant reference value θ_o and the constants g and Ω are the gravity acceleration and angular rotation rate respectively.

Two conditions need to be satisfied in order that this extremum be a minimum:

A) The square of the angular momentum $M(= vr + \Omega r^2)$ should increase with radius along isentropic surfaces.

B) The static stability should be positive

Equation (1) can be written in terms of the angular momentum as:

$$\frac{M^2}{r^3} = \frac{\partial}{\partial r} (\phi + \frac{1}{2} \Omega^2 r^2)$$

which may be simplified to:

$$M^2 = \frac{\partial P}{\partial R} \qquad (3)$$

on introducing the new radial coordinate R given by

$$R = \frac{1}{2} (\frac{1}{r_o^2} - \frac{1}{r^2}) \qquad (4)$$

where r_o is a constant and letting $P = \phi + {}^1/_2 \Omega^2 r^2$; the hydrostatic equation (2) becomes

$$\frac{g\theta}{\theta_o} = \frac{\partial P}{\partial z} \quad . \qquad (5)$$

Since R increases monotonically with increasing r, condition A requires that:

$$(\frac{\partial M^2}{\partial R})_\theta > 0$$

where the subscript indicates that differentiation is along an isentropic surface. Conditions A and B are both satisfied if the matrix

$$\begin{pmatrix} \frac{\partial M^2}{\partial R} & \frac{\partial M^2}{\partial z} \\ \frac{g}{\theta_o} \frac{\partial \theta}{\partial R} & \frac{g}{\theta_o} \frac{\partial \theta}{\partial z} \end{pmatrix}$$

is positive-definite
(ie has positive eigenvalues)

since, as shown by Shutts and Cullen (1987), this implies that:

$$\frac{\partial \theta}{\partial z} > 0 \text{ and } J (\frac{M^2, \theta}{R, z}) > 0$$

or $$J (\frac{M^2, \theta}{R, \theta}) \cdot J(\frac{R, \theta}{R, z}) = (\frac{\partial M^2}{\partial R})_\theta \cdot \frac{\partial \theta}{\partial z} > 0 \cdot$$

Using eqs (3) and (5), conditions A and B are therefore satisfied if the Hessian matrix

$$\begin{pmatrix} \frac{\partial^2 P}{\partial R^2} & \frac{\partial^2 P}{\partial R \partial z} \\ \frac{\partial^2 P}{\partial R \partial z} & \frac{\partial^2 P}{\partial z^2} \end{pmatrix}$$

is positive-definite.

In the context of semi-geostrophic theory, Cullen and Purser (1984) recognised that this positive definite requirement has a simple geometrical interpretation; that is, that the surface P is convex when viewed from below. Furthermore, they proposed that fronts are simply 'creases' in this surface where the gradient of P changes discontinuously. From this viewpoint the convexity requirement is a stronger statement of the minimum energy condition than the positive definiteness of the Hessian matrix.

b. The element model

Any inertially and convectively stable axisymmetric flow can be characterised by a convex modified pressure P(R,z) related to the geopotential by:

$$P(R,z) = \phi + \frac{1}{4} \frac{\Omega^2}{R_o - R} \qquad (6)$$

where $R_o = {}^1/({}_2\, r_o{}^2)$.

If the M^2 and θ fields are approximated by N elements of known mass, each of which is homogeneous in the same variables, then the P function is represented by a convex multi-facetted shell defined by

$$P(R,z) = \max_{i=1,N} \{M_i^2 R + \frac{g\theta_i z}{\theta_o} + S_i\} \qquad (7)$$

where M_i^2 and θ_i are the squared angular momentum and potential temperature of the ith element respectively and S_i are a set of constants. Each element is associated with a plane defined in the Cartesian space with co-ordinates (R, z, P). S_i effectively determines the height of the plane associated with element i above the (R,z) plane. The projection of the lines of intersection of the planes in the convex shell onto the (R,z) plane defines the stable element geometry. All elements are convex polygons. Cullen and Purser prove that the S_i values can always be adjusted so that the areas of these polygons correspond with the assumed masses of the elements. In their proof, mass is equated to area; here the mass corresponding to a given element polygon in the (R,z) plane is a complicated function of the vertex co-ordinates.

The proof rests on the fact that if P is a convex surface then increasing the 'S' value of a single element will always result in a new polygon which entirely contains the 'old' polygon: the area of the element therefore always increases as S increases - at the expense of the neighbouring elements. Similarly, the mass of the 'new' polygon in the (R,z) plane always exceeds the mass of the enclosed 'old' polygon on raising the value of S associated with an element and so the proof can be trivially extended to the axisymmetric case.

Denoting the mass or volume of element i by V_i then it can be shown that:

$$V_i = \frac{\pi}{2} \int_{D_i} \frac{dRdz}{(R-R_o)^2} \qquad (8)$$

where D_i is the region of (R,z) plane occupied by element i. V_i is calculated by dividing D_i into triangles and using an analytic expression for the volume associated with a triangle in the (R,z) plane obtained from the integral in eq. (8) (see Appendix). With this relation and the co-ordinate transformation it was possible to adapt the semi-geostrophic, Geometric model code developed by Chynoweth (1987) (also outlined in Cullen et al, 1987). The only other change required to complete the transformation from two-dimensional semi-geostrophic model to axisymmetric Geometric model was in the area or volume iteration process described in Cullen et al (1987) which adjusts the volumes of elements to their correct value. This proceeds by repeatedly applying the Newton method represented here by:

$$V_i^* - V_i = \left(\left(\frac{\partial V_i}{\partial S_j} \right)\right) (S_j^* - S_j) \qquad (9)$$

where V_i^* are the approximate volumes calculated from the element geometry obtained using S_j^* and $\partial V_i/\partial S_j$ is the sparse matrix of coefficients describing how the volumes change with S_i. Eq. (9) is solved at each iteration step for S_j which are then used to construct a new geometry; iteration is stopped when the desired accuracy in V_i^* is achieved. The coefficients $\partial V_i/\partial S_j$ may be evaluated as follows.

Consider the boundary between elements i and j as depicted in Fig. 1. The shaded strip corresponds to the increase in area of element i at this interface as $S_i \rightarrow S_i + \delta S_i$. If u is a co-ordinate along the interface and ψ is the slope angle of the interface as shown in Fig. 1, then:

$$\delta V_i = \delta_{ij} \int_0^{\pi} \frac{du}{2\,(R-R_o)^2} = \frac{\pi\,\delta_{ij}}{2\,\mathrm{Cos}\,\psi} \int_{R_1}^{R_2} \frac{dR}{(R-R_o)^2} \qquad (10)$$

where δ_{ij} is the width of the strip and R_1 and R_2 correspond to the endpoints of the element interface. The axisymmetric equivalent of Margules' formula for the slope of an element interface is given by:

$$\mathrm{Tan}\,\psi = \frac{dz}{dR} = -\frac{\theta_o[M^2]}{g\,[\theta]} \qquad (11)$$

using eqs. (3) and (5) and where [ ] denotes the difference across an element boundary; therefore it is easily shown that for the case under consideration

$$\mathrm{Cos}\,\psi = -\frac{g(\theta_i - \theta_j)/\theta_o}{\sqrt{(g[\theta_i-\theta_j)/\theta_o]^2 + (M_i^2-M_j^2)^2}} \qquad (12)$$

Substituting eq. (12) into eq. (10) and evaluating the integral gives:

$$\delta V_i = \frac{\theta_o \pi \delta_{ij}}{2g(\theta_i-\theta_j)} \{(M_i^2-M_j^2)^2 + (g(\theta_i-\theta_j)/\theta_o)^2\}^{1/2} \cdot \frac{(R_2-R_1)}{(R_1-R_o)(R_2-R_o)} \qquad (13)$$

It can be shown (Cullen et al, 1987) from simple geometrical considerations that

$$\frac{\delta_{ij}}{\delta S_j} = \frac{1}{\{(M_i^2 - M_j^2)^2 + \left(\frac{g(\theta_i - \theta_j)}{\theta_o}\right)^2\}^{1/2}}$$

and so, dividing eq. 13 by δS_j and taking the limit $\delta S_j \to o$ gives

$$\frac{\partial V_i}{\partial S_j} = \frac{\pi\theta_o}{2g(\theta_i - \theta_j)} \cdot \frac{(R_2 - R_1)}{(R_1 - R_o)(R_2 - R_o)} \qquad (14)$$

for $i \neq j$.

Note also that

$$\frac{\partial V_i}{\partial S_i} = - \sum_{j \text{ (neighbours)}} \frac{\partial V_i}{\partial S_j} \qquad (15)$$

consistent with the symmetry of the matrix $\partial V_i / \partial S_j$ and the requirement that the gain in volume of element i equals the sum of the losses in volume of its neighbours.

A time dependent problem involving heat and momentum forcing can be solved by calculating at each time step, new sets of M_i and θ_i and constructing the new element geometry using the previous time step values of S_i as a first guess. The iteration technique for correcting element volumes typically involves four or five steps to achieve less than 1% error on all elements.

3. Penetrative convection experiments

Consider a horizontally-stratified annular region (inner radius r_o= 5 km and outer radius $r_* = 300$ km) of atmosphere in solid rotation ($\Omega = 6 \times 10^{-5}$ s^{-1}) with horizontal plane boundaries at z=0 and z=10 km. A constant static stability B ($\theta_o^{-1} d\theta/dz$) is chosen with value 1.67×10^{-5} m^{-1} consistent with a 50 K potential temperature difference between the top and bottom of the model atmosphere and with $\theta_o = 300$ K.

v is chosen to be zero so that initially

$$M^2 = \Omega^4 r^2 = \frac{\Omega^4}{2(R_o - R)} = \frac{\partial P}{\partial R} \qquad (16)$$

and $\frac{\theta}{\theta_o} = 1 + Bz$ which implies:

$$\frac{\partial P}{\partial z} = g(1 + Bz) \qquad (17)$$

using eq. 5.

Eqs. (16) and (17) define, to within an arbitrary constant, a continuous P surface. This may be approximated by the convex shell represented by:

$$P(R,z) = \max_{i=1,N} \{M_i^2 R + \frac{g\theta z}{\theta_o} + S_i\}$$

over the domain indicated above. A discretization is obtained by dividing the domain (r, z) into a regular rectangular grid and evaluating P, M_i and θ_i at the centre (R_i, z_i) of each rectangle, and then using eq. (7) to determine a first guess for S_i. Newton iteration is then carried out so that the S_i values are adjusted until the correct volumes of the elements

are obtained. Fig. 2(a) shows an initial state obtained in this way. The domain is divided into 24 x 24 elements with two different sizes in (r, z) space: small elements of 5 km width within a radius of 100 km and an outer region with elements of width 40 km. The height of all elements initially is 5/12 km. Since all interfaces are straight lines in (R, z) space, they become curves in (r, z) in accordance with eq. (4). In fact, these characteristic curves are simply the M and θ surfaces of the zero potential vorticity model of Shutts (1981). All of our results will be plotted in the (r, z) plane choosing enough points within interfaces to correctly define their shape. At the resolution adopted here these, for the most part, appear as straight lines.

Consider the group of elements which are shaded in Fig. 2(a). We shall suppose that they are saturated and have enough convective available potential energy (CAPE) to allow them to be positively buoyant up to some level at which their potential temperature is θ_*. The object of the experiment is to find the new equilibrium state after the cylindrical region, represented by the shaded elements, has convected. Angular momentum is assumed to be conserved following these toroidal elements. Heating a single element causes the slope of the corresponding plane making up the P surface to increase which, with the same value of S, leads to an increase in the element's area. S has to be decreased therefore by an amount depending on how large a potential temperature increment an element receives. Elements making up the shaded region are heated one at a time and a sequence of balanced states is obtained.

It is intructive to examine the balanced flow states corresponding to different depths of heated elements as they are found in the above calculation. Shutts (1987) found that for rectilinear flow, the character of the final balanced flow in the vicinity of the region of heating depends strongly on the aspect ratio of the region. In particular, for a 'tall' ellipsoidal heating region with aspect ratio $N/2\Omega$ x greater than unity, a vertical front is obtained. Fig. 3(a) shows the balanced state corresponding to the convection of the shaded elements in Fig. 2(a). As found in the equivalent rectilinear problem (Shutts (1987)) the 'convected elements' form a lens at the level of neutral buoyancy; elements immediately above (below) this lens are lifted (forced down). The 'hole' formed by removing these two layers of elements causes subsidence and radial contraction of adjacent elements. Note that the areas of elements in the (r, z) plane increase as they move to smaller radii since element volumes are conserved.

Contrast this state with the balanced flow states (Figs. 3(b) and (c)) resulting from the convection of the shaded elements in Figs. 2(b) and (c). As the aspect ratio of the cylinder of air removed by convection gets larger so the width of the funnel of potentially warm air sucked down decreases. Unlike the rectilinear, semi-geostrophic problem, the removal of a tall, solid cylinder of air cannot create a vertical front since air bounding this cylinder will have finite angular momentum and, on contraction to the axis of the cylinder, would rotate at infinite speed. Instead, air from near the top of the cylinder (if bounded from below by a rigid plane surface) is sucked down and a curved frontal discontinuity surface is formed at finite radius. The reality of such a front can be

demonstrated by plotting the pressure (or geopotential) perturbation as a function of radius for a given level; this is easily computed from the modified pressure P using the defining equation $P = \phi + {}^1/_2\ \Omega^2 r^2$. The surface pressure perturbation graphs set beneath the element configurations in Fig. 3(a)-(c) were evaluated by calculating ϕ at points equally spaced, with separation of about 3 km: no smoothing has been applied. The geopotential perturbation is related to pressure by taking the density of air to be 1 kg m^{-3}. Note that the element resolution is sufficiently coarse at radii greater than 100 km for the piecewise differentiable nature of the pressure to be plainly evident. The frontal boundary in Fig. 3(a) between the air which has subsided and that which has moved along the lower boundary is marked by a pronounced slope discontinuity in the pressure perturbation at a radius of 12 km. In Fig. 3(b), the flattening of the surface pressure gradient within the radius of the discontinuity is not resolved and in Fig. 3(c) the front has collided with the inner boundary. Similar pressure perturbation plots at higher levels can be used to identify the position and extent of the front. By analogy with the intense gradients which bound the hurricane warm core, this discontinuity surface will be called the eyewall front.

Tangential velocity fields associated with Figs. 3(a)-(c) are shown in Figs. 4(a)-(c). These were hand-drawn using values calculated at element centroid positions and pressure perturbation plots to locate the eyewall front and to estimate the maximum wind speed near the front. No reliable method for machine contouring fields derived from the Geometric models has yet been found which does not introduce spurious 'wobbles' or which does

not degrade the information in the model. Most contouring routines assume smooth, differentiable fields: model discontinuities are therefore unpalatable to them.

As can be deduced from the pressure perturbation plot in Fig. 3(a) the maximum tangential wind occurs at the outer side of the eyewall front with speed $\simeq$ 10 ms^{-1} at a radius of 12 km. The lens is characterized by anticyclonic flow with a peak speed of over 3 ms^{-1} at a radius of 90 km (Fig. 4(a)). The eyewall front occurs at smaller radius in Fig. 4(b) and has a marked tilt outwards with height. Peak speeds for the low level cyclonic and upper level anticyclonic flow are 14 and 5 ms^{-1} and are attained at r = 8 km and 112 km respectively. For the large aspect ratio case (Fig. 3(c)) the eyewall front flares outwards to a radius of over 30 km at a height of about 2.6 km: lower down it collides with the inner wall suggesting that with smaller r_o, the surface front would occur at a radius less than 5 km. The cyclonic vortex now has speed approaching 20 ms^{-1} which supports a potential temperature contrast across the eyewall front of 10 K. The lens extends out to 125 km where an anticyclonic flow of 6 ms^{-1} is achieved. Notice that in all three cases the lens is bounded above and below by layers of intense vertical shear and, at its outer rim, by intense cyclonic vorticity. Similar features are to be found in the analytic lens solutions of Gill (1981) and Shutts (1987). The displacement vectors of element centroids resulting from the convection in the three cases is shown in Figs. 5(a)-(c). These show more clearly than the element pictures themselves, the pattern of forced subsidence into the cyclonic vortex and below the lens with forced ascent above the lens. The small vector displacements midway between lens and vortex in Figs 5(a) and (b) show that

their respective circulations are to a large degree uncoupled for the parameter values chosen here. In Fig. 5(c) it can be seen that subsidence is apparent throughout the mid-levels indicating a small degree of coupling. The surface central pressure perturbation is rather small in all of the above examples ($\simeq$ 3 mb) yet the small horizontal scale (10-20 km) of the corresponding vortices implies strong winds.

A final experiment in this series was carried out to compare the effect of different aspect ratios of the heated region given the same amount of convective mass transfer. Fig. 6(a) shows the elements to be convected; their total mass is equal to that convected in the last of the previous experiments (c.f. Fig. 2(c)). The potential temperature of the shaded elements again is increased to θ_* and the resulting element configuration is shown in Fig. 6(b). Since the larger aspect ratio region contains a smaller range of angular momentum, the resulting lens is slightly squatter than that in Fig. 6(b). The warm core 'funnel' of Fig. 3(c) is absent with only a shallow front forming in the air bounding the outer edge of the heating region initially.

The very small horizontal scale of the vortices resulting from the above convective mass transfer experiments put them in the league of tornado-cyclones rather than hurricanes, polar lows and extratropical depressions. In order to get some insight into the equivalent larger scale problem and to examine the effects of downdraughts generated by evaporational cooling, the following two experiments were set up.

Fig. 7(a) shows the initial element geometry for these experiments for which the resolution is uniform in (r,z) space and the annular domain extends from an inner wall at 50 km to an outer wall at 1000 km. The depth of the domain and vertical increment of potential temperature were chosen to be identical to the previous experiments. Ω was set equal to 3×10^{-5} s^{-1} - equivalent to a motionless atmosphere at a latitude of 24°. The region of shaded elements in Fig. 7(a) extends out to a radius of 317 km and has a depth of 1.25 km. As before these are heated so that they form a lens at a height of 7 km with elements each conserving their total angular momentum. Although the qualitative form of the resulting balanced flow (Fig. 8(a)) is similar to that in Fig. 3(a) the ratio of the eyewall front radius to the radius of the outer rim of the lens is much larger ($^2/_5$ compared with $^1/_9$ for Fig. 3(a)). The surface pressure plot reveals a central zone of weak gradient extending to the eyewall front at 175 km. Within this region the pressure and potential temperature anomalies are approximately -3.5 mb and +6 K respectively and decrease rapidly with height. The tangential velocity field (Fig. 9(a)) shows an intense low level wind maximum of 17 ms^{-1} at the base of the eyewall front and an anticyclonic flow maximum of 6 ms^{-1} at a radius of 510 km. The centroid displacement vectors (Fig. 10(a)) indicate substantial forced descent throughout the region between lens and eyewall front.

Since deep convection is invariably accompanied by the production of cool downdraughts through evaporational coding (or melting of frozen precipitation) in middle or lower troposphere it was decided to imitate this effect by cooling a group of elements (stippled region of Fig. 7(b)) following on from the heating experiment just described. Note that the

resulting balanced state does not depend on the order in which elements are heated or cooled. The eight elements making up the stippled region were cooled to a potential temperature 2 K lower than the initial potential temperature of the surface elements: Fig. 8(b) shows the element configuration that results. The cold 'downdraught' air forms a dome which undercuts the air which has subsided in response to upward convective mass transfer of the shaded elements, thereby creating an intense inversion. The potential temperature increases by 8 K across this inversion. Another frontal discontinuity is created above the dome and attached to the inner boundary as air descends in response to the effective mass sink associated with the stippled elements. Frontal surfaces also exist at the leading edge of the cold out flow dome which, together with the inversion, form a reversed 'y' shape.

An increase in surface pressure of about 2 mb has resulted from the weight of the cold air dome and the eyewall front has been pushed out to a radius of 240 km at the surface. The discontinuity in pressure gradient associated with the surface front is clearly defined in the model. A complex pattern of tangential velocity (Fig. 9(b)) emerges with a weakened cyclonic wind maximum of 12 ms^{-1}; another cyclonic maximum above the dome at the inner boundary, and anticyclonic flow in the cold air dome with maximum speed $\simeq$ 4 ms^{-1} on the inner side of the surface front. The velocity field in the lens is barely changed.

It is interesting to compare qualitatively the structure of the vortex, lens and cold dome of the last experiment with cross-sections through a vortex embedded in a mesoscale convective complex simulated using

a nested three-dimensional primitive equation model (Zhang and Fritsch, 1987). Both show a warm-cored cyclone above a dome of cold air created by downdraughts and beneath an outflow anvil of low absolute vorticity. Zhang and Fritsch also note adiabatic cooling immediately above the outflow level consistent with the forced ascent above the lens in the Geometric model. Cyclonic vorticity extended up to the base of the outflow layer in their experiment implying an effective mass sink over a deeper layer than in our experiment.

4. Discussion

The main feature of the Geometric model highlighted in section 3 is its ability to represent convective stabilization through penetrative mass transfer. No numerical diffusion is required in the model. We have shown how penetrative convection in a rotating, stratified vortex can generate a low-level warm-cored cyclone and create a lenticular region of anticyclonic vorticity at the level of neutral buoyancy. Between these levels air subsides and would tend to remove the initial convective available potential energy.

Perhaps the most restrictive assumption of the model is that of axisymmetry. It is clear from many observational studies that zones of intense convection are frequently organized in curved bands in the forward sector of travelling depressions (Reed and Albright, 1986). Polar lows also appear to have important non-axisymmetric aspects to their structure (Shapiro et al, 1987). We have the choice in these situations of either regarding the model results presented here as being applicable in the

convectively active sector of the system, or of considering the model to represent the azimuthal-mean circulation. From both viewpoints, parcel conservation of angular momentum will not hold with any degree of precision though this is unlikely to detract from the qualitative predictions of lens and eyewall front: the lens is caused by mass transfer. In fact there is some observational evidence that momentum is approximately conserved in the updraught of middle-latitude squall lines (Ogura and Liou, 1980). If, on the other hand, air parcels experience an increase in angular momentum then the lens would be displaced to greater radii.

Another major assumption of the model results shown here is that of no mixing. The balanced flow states prediced are only relevant to vortices within which convection is predominantly penetrative. Nevertheless, entrainment/detrainment could be parametrized in the model by transferring heat and momentum across element interfaces without disrupting the integrity of the element geometry. For instance, heat transfer from one element to a neighbour might be proportional to their difference in potential temperature. Allowing for the different masses (and therefore thermal capacities) of the elements, potential temperature increments could be calculated after a certain time.

If the model predictions are to be related to real convective situations, enough time must have elapsed for the cyclostrophic adjustment process to have taken place. The time scale for cyclostrophic adjustment (τ_c) is approximately given by the inverse of the inertial stability

$$\left(\frac{2v}{r} + f\right)^{1/2} \cdot \left(\frac{1}{r}\frac{\partial(vr)}{\partial r} + f\right)^{1/2}$$

where f is the Coriolis parameter (Schubert and Hack, 1982).

In situations where convective mass transfer is still 'pumping up' the lens, we might expect the Geométric model's prediction to be meaningful if (say) 90% of the mass composing the lens has been there for a time longer than τ_c. Within a time τ_c after the onset of convection, the outflow anvil will probably be squat compared to the equivalent balanced lens shape though this will depend on the fate of the excess kinetic energy of the updraught at the neutral buoyancy level.

The formation of warm cores in cyclonic weather systems that are initially cold is well known to coincide with the onset of deep convection. Frequently these vortices develop a cloud-free 'eye' similar in appearance to those associated with hurricanes. Rasmussen (1979) argued that the spiral cloud formations of polar lows is evidence of a similar underlying role of convection to that in tropical storms.

In a later paper (Rasmussen, 1985) he presents a case study of a polar low which developed from an upper level cold core cyclone. Deep convection was instrumental in the evolution of an intense warm core depression in the lower troposphere. Aircraft flights through a polar low during the recent Arctic Cyclone Expedition were reported by Shapiro et al (1987). Their analysis of the mesoscale structure of a polar low - which was based on in-flight measurements, dropsonde profiles and radiosonde ascents - showed a pronounced warm core bounded (at least on one side) by a steep front reminiscent of that forced by penetrative convection in the Geometric model.

The inner core of extratropical depressions frequently takes on hurricane-like characteristics when the development is 'explosive' (Sanders and Gyakum, 1980; Bosart (1981)). Depressions with hurricane-like appearance in satellite imagery have been reported over the Mediterranean in autumn and winter (Ernst and Matson, 1983; Mayengon, 1984) and were accompanied by vigorous convection. In a case study of 'the Queen Elizabeth II' storm, Gyakum (1983(a), (b)) shows that the explosive development of the surface low was coincident with the appearance of deep convection identified by the growth of anvil cirrus in satellite imagery. The warming of the lower troposphere (25-35K) and formation of a thickness (1000-250 mb) maximum at the depression core was argued to be the result of cumulus-induced subsidence. Gyakum (1983b) attempted (using a quasi-geostrophic model) to calculate the deepening due to convective heating by estimating the diabatic modification to the potential vorticity field. The Geometric model experiments of the previous section represent the same physical problem yet differ from Gyakum's calculation in a fundamental manner. The heating function used by Gyakum represents the combined influence of latent heating and subsidence-induced warming on the synoptic scale flow; in the Geometric model the heating effect comes entirely from explicitly-modelled subsidence warming associated with convective mass transfer. The potential vorticity of air parcels which do not convect is unchanged in the after-state, in contrast to the calculated change in Gyakum's model though the eyewall front constitutes a line source of potential vorticity. Although both calculations give the same overall picture, differences in detail concern the balanced flow in and near the lens and eyewall front of the Geometric model.

Another comprehensive case study of an explosive cyclogenesis event was carried out by Reed and Albright (1986). They came to similar conclusions as Gyakum regarding the role of convection in the deepening of the depression and furthermore showed that the accompanying frontal cloud band was highly symmetrically unstable. Again, the study presented evidence of a warm core structure and intense subsidence behind the main organised convective band. It should be stressed, however, that warm core cyclones may be generated by other mechanisms. Warm air may be 'secluded' in the final stages of baroclinic development (Shapiro et al, 1987).

The Geometric model has been used here in a purely diagnostic mode. Nevertheless it would be possible to incorporate physical parametrization of surface friction and surface heat exchange so that the model could be used for time dependent problems. Each element would conserve some average value of equivalent potential temperature so that moist (slantwise) convection could be initiated by lifting associated with frictional convergence. In contrast to other 'CISK' models (Charney and Eliassen, 1964), the effect of convection would be explicitly represented as a penetrative mass transfer process and no heating function would need to be specified. Of course, in real convective systems cool downdraughts driven by evaporation of precipitation into air of low equivalent potential temperature accompany the updraughts. As shown in the last of our experiments, these too can be catered for explicitly though no attempt has been made here to parametrize the detailed microphysical and thermodynamic processes.

Since the area of the lens in our experiments is an indicator of the total mass transported in the convective updraught, it would be tempting to relate this to the area of convective anvil tops identifiable in satellite pictures. The Geometric model could be used to relate lens area to the fall of surface pressure in the vortex which could then be verified against the observed explosive deepening accompanying the growth of anvil tops. In practise the contribution of cool downdraughts to the raising of surface pressure might detract from the usefulness of such an assumed relationship.

5. Summary and Conclusions

A Geometric construction method of finding balanced axisymmetric vortex states, given the angular momentum, potential temperature and mass of a set of toroidal elements, has been described. The existence of convectively and inertially stable flow states in gradient wind and hydrostatic balance is guaranteed by the convexity of a certain modified pressure function when the radial co-ordinate (r) is transformed to R in accordance with the formula

$$R = \frac{1}{2}\left(\frac{1}{r_o^2} - \frac{1}{r^2}\right)$$

where r_o is a constant. The main strength of this technique over standard partial differential equation solvers for finding balanced states (consistent with a certain potential vorticity distribution) is that impulses of heat or momentum may be applied to any subset of elements and the model provides one with a new balanced state on the assumption of no mixing. The equivalent invertibility problem (Hoskins et al, 1985; Thorpe,

1986) would require additional assumptions since the potential vorticity above the region where heat is injected would become negative implying a symmetrically unstable state. One assumption would be that mixing (say along angular momentum surfaces) brings about neutrality to slantwise instability. The Geometric model implicitly assumes parcel conservation of potential temperature and angular momentum.

The model is therefore ideal for studying the cyclostrophically adjusted flow states resulting from penetrative convection. It could be used to model hurricanes, polar lows and some aspects of explosive cyclogenesis. We have shown that the main effect of the mass transfer associated with convection is to produce a mesoscale lens at upper levels (which may be identified with the cirrus anvil of real convective outflows) and a warm-cored cyclone at lower levels bounded by an 'eyewall front' which separates the warm air forced downwards near the axis of rotation from the cooler surface air at larger radii. The case studies of Gyakum (1983a) and Reed and Albright (1986) provide observational support for this picture with subsidence warming alongside deep convection accounting for the dry, warm-core eye of the storm.

Acknowledgements

We are grateful to Drs M J P Cullen, L Uccellini and R J Purser for useful discussion and to Mr M Holt for help with the Geometric model computer code.

Legends

Fig. 1. Schematic diagram showing element interfaces (solid lines) and the increase in area of element i at the interface between elements i and j (shaded strip) due to a small increase in S_i.

Fig. 2(a)-(c) Initial element representation of an atmosphere at rest with static stability $B = 1.67 \times 10^{-5}\ m^{-1}$ and $\Omega = 6 \times 10^{-5}\ s^{-1}$ for the three experiments showing in (a)-(c) the elements to be heated (shaded). Elements within horizontal layers have the same potential temperature; layer values of θ increase upwards in steps of 2.1 K. Elements with vertical columns have the same angular momentum.

Fig. 3. (a)-(c) Element geometries after the shaded elements in corresponding Figs. 2(a)-(c) have convected. The shaded region indicates the elements which have been heated. The bold line indicates the position of the eyewall front. Graphs of surface pressure perturbation (mb) are set below the element pictures. The perturbation is defined to be zero at the outer edge of the domain.

Fig. 4(a)-(c) Tangential velocity fields associated with Figs. 3(a)-(c) contoured every 1 ms^{-1} except (c) for which the interval is 2 ms^{-1}.

Fig. 5(a)-(c) Centroid displacement vectors corresponding to Figs. 3(a)-(c).

Fig. 6(a) Initial state and elements to be heated (shaded) for the low aspect ratio experiment.

(b) Element geometry resulting from the convection of the shaded elements in Fig. 6(a).

Fig. 7(a)-(b) Initial element geometries for the larger scale convective mass transfer experiments. In (b), the stippled region is to be cooled.

Fig. 8(a)-(b) The final states after the corresponding shaded elements in Fig. 7(a) and (b) have convected with surface pressure perturbation set below. Bold lines correspond to frontal surfaces.

Fig. 9(a)-(b) Tangential velocity contours corresponding to Figs. 8(a) and (b) in ms^{-1}.

Fig. 10(a)-(b) Displacement vectors corresonding to Figs. 8(a) and (b).

Fig. 11 Schematic diagram showing the triangular region in the (R,z) plane referred to in the Appendix.

Appendix

Evaluation of the element volume whose cross-section is triangular in the (R,z) plane.

Consider the triangle depicted in Fig. 11 with vertices at $(R_1\ z_1)$, $(R_2\ z_2)$ and $(R_3\ z_3)$. The straight lines forming the sides of the triangle have equations

$$h_1(R) = \alpha_{13}R + \beta_{13}$$
$$h_2(R) = \alpha_{12}R + \beta_{12}$$
$$h_3(R) = \alpha_{23}R + \beta_{23}$$

where $\alpha_{ij} = \dfrac{z_j - z_i}{R_j - R_i}$ and $\beta_{ij} = z_j - R_j\,\alpha_{ij}$.

The volume of the torus (V_t) in physical space corresponding to the triangle is, using eq. 25

$$V_t = \int_{R_1}^{R_2}\int_{h_1(R)}^{h_2(R)} f(R)\,dR\,dz + \int_{R_2}^{R_3}\int_{h_1(R)}^{h_3(R)} f(r)\,dR\,dz \qquad (A)$$

where $f(R) = \dfrac{\pi}{2(R_o - R)^2}$.

Letting

$$h_2(R) - h_1(R) = K_1 R + C_1$$
$$h_3(R) - h_1(R) = K_2 R + C_2$$

and

$$V_t = V_t^{(1)} + V_t^{(2)}$$

where $K_1 = \alpha_{12} - \alpha_{13}$

$K_2 = \alpha_{23} - \alpha_{13}$

$C_1 = \beta_{12} - \beta_{13}$

and $C_2 = \beta_{23} - \beta_{13}$ then:

$$V_t^{(1)} = \frac{\pi}{2}\int_{R_1}^{R_2} \frac{K_1R + C_1}{(R_o-R)^2}\, dR \quad \text{and} \quad V_t^{(2)} = \int_{R_2}^{R_3} \frac{K_2R + C_2}{(R_o-R)^2}\, dR \qquad (B)$$

Expressions (B) involve standard integrals and can be shown to lead to:

$$V_t^{(1)} = \frac{(C_1 + K_1 R_o)(R_2-R_1)}{(R_o-R_2)(R_o-R_1)} + K_1 \ln\left(\frac{R_o-R_2}{R_o-R_1}\right)$$

and $$V_t^{(2)} = \frac{(C_2 + K_2 R_o)(R_3-R_2)}{(R_o - R_3)(R_o-R_2)} + K_2 \ln\left(\frac{R_o-R_3}{R_o-R_2}\right)$$

References

Bosart, L.F. (1981) 'The Presidents' Day snowstorm of 18-19 February 1979: A subsynoptic-scale event'. Mon. Wea. Rev., 109, 1542-1566.

Charney, J.G. and A. Eliassen (1964) 'On the growth of the hurricane depression'. J. Atmos. Sci., 21, 68-75.

Chynoweth, S. (1987) 'The semi-geostrophic equations and the Legendre transformation'. Ph.D. Thesis, Dept. of Mathematics, Univ. of Reading, England.

Cullen, M.J.P. (1983) 'Solutions to a model of a front forced by deformation'. Quart. J. Roy. Met. Soc., 109, 565-573.

Cullen, M.J.P. and R.J. Purser (1984) 'An extended Lagrangian theory of semi-geostrophic frontogenesis'. J. Atmos. Sci., 41, 1477-1497.

Cullen, M.J.P., S. Chynoweth, R.J. Purser (1987) 'On some aspects of flow over synoptic scale tropography'. Quart. J. Roy. Met. Soc., 113, 103.

Eliassen, A. and E. Kleinschmidt (1957) 'Dynamic Meteorology'. Handbuch der Physik, Geophysik II, Springer-Verlag.

Ernst, J.A. and M. Matsum (1983) 'A Mediterranean tropical storm?' Weather, 38, 332-337.

Fjortoft, R. (1946) 'On the frontogenesis and cyclogenesis in the atmosphere'. Part I. On the stability of the stationary circular vortex. Geofys. Publik., 16 (5), 1-28.

Gill, A.E. (1981) 'Homogeneous intrusions in a rotating stratified fluid'. J. Fluid Mech., 103, 275-295.

Gill, A.E., J.M. Smith, P. Cleaver, R. Hide and P. Jonas (1979) 'The vortex created by mass transfer between layers of a rotating stratified fluid'. Geophys. Astrophys. Fluid Dyn., 12, 195-220.

Gyakum, J.R. (1983a) 'On the evolution of the QE II storm. I: Synoptic aspects. Mon. Wea. Rev., 111, 1137-1155.

Gyakum, J.R. (1983b) 'On the evolution of the QE II storm. II: Dynamics and thermodynamic structure. Mon. Wea. Rev., 111, 1156-1173.

Hoskins, B.J. and F.P. Bretherton (1972) 'Atmospheric frontogenesis models: mathematical formulation and solution. J. Atmos. Sci., 29, 11-37.

Hoskins, B.J., M.E. McIntyre and A.W. Robertson (1985) 'On the use and significance of isentropic potential vorticity maps'. Quart. J. Roy. Met. Soc., 111, 877-946.

Mayengon, R. (1983) 'Warm core cyclones in the Mediterranean'. Mariners Wea. Log. 28, 6-9.

Ogura, Y. and Liou, M-T (1980) 'The structure of a mid-latitude squall line: a case study'. J. Atmos. Sci., 37, 553-567.

Rasmussen, E. (1979) 'The polar low as an extratropical CISK disturbance'. Quart. J. Roy. Met. Soc., 105, 531-549.

Rasmussen, E. (1985) 'A case study of a polar low development over the Barents Sea'. Tellus, 37A, 407-418.

Reed, R.J. and M.D., Albright (1986) 'A case study of explosive cyclogenesis in the Eastern Pacific'. Mon. Wea. Rev. 114, 2297-2319.

Sanders, F. and Gyakum, J.R. (1980) 'Synoptic-dynamic climatology of the 'bomb''. Mon. Wea. Rev., 108, 1589-1606.

Schubert, W.H. and Hack, J.J. (1982) 'Inertial stability and tropical cyclone development'. J. Atmos. Sci., 39, 1687-1697.

Schubert, W.H. and Hack, J.J. (1983) 'Transformed Eliassen balanced vortex model'. J. Atmos. Sci., 40, 1571-1583.

Shapiro, M.A., L.S. Fedor and T. Hampel (1987) 'Research aircraft measurements of a polar low over the Norwegian Sea'. Tellus, 39A, 272-306.

Shapiro, L.J. and Willoughby, H.E. (1982) 'The response of balanced hurricanes to local sources of heat and momentum'. J. Atmos. Sci., 39, 378-394.

Shutts, G.J. (1987) 'Balanced flow states resulting from penetrative slantwise convection'. J. Atmos. Sci., 44, 3363-3376.

Shutts, G.J. (1981) 'Hurricane structure and the zero potential vorticity approximation'. Mon. Wea. Rev., 109, 324-329.

Shutts, G.J. and M.J.P. Cullen (1987) 'Parcel stability and its relation to semi-geostrophic theory'. J. Atmos. Sci., 44, 1318-1330.

Smith, R.K. (1981) 'The cyclostrophic adjustment of vortices with application to tropical cyclone modification'. J. Atmos. Sci., 38, 2021-2030.

Thorpe, A.J. (1986) 'Synoptic scale disturbances with circular symmetry'. Mon. Wea. Rev., 114, 1384-1389.

Zhang, D-L and Fritsch, J.M. (1987) 'Numerical simulation of the meso-β scale structure and evolution of the 1977 Johnstown Flood. Part II: Inertially stable warm-core vortex and mesoscale convective complex'. J. Atmos. Sci., 44, 2593-2612.

Fig. 1

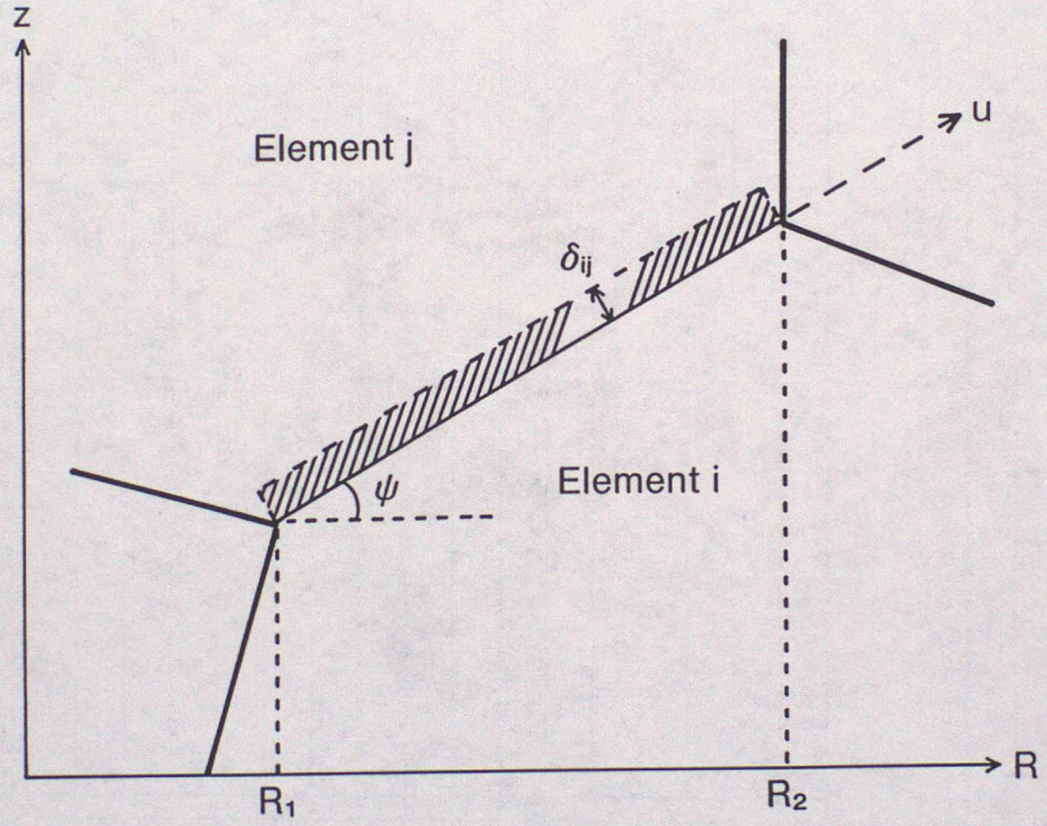

Fig. 2(a)

Fig. 2(b)

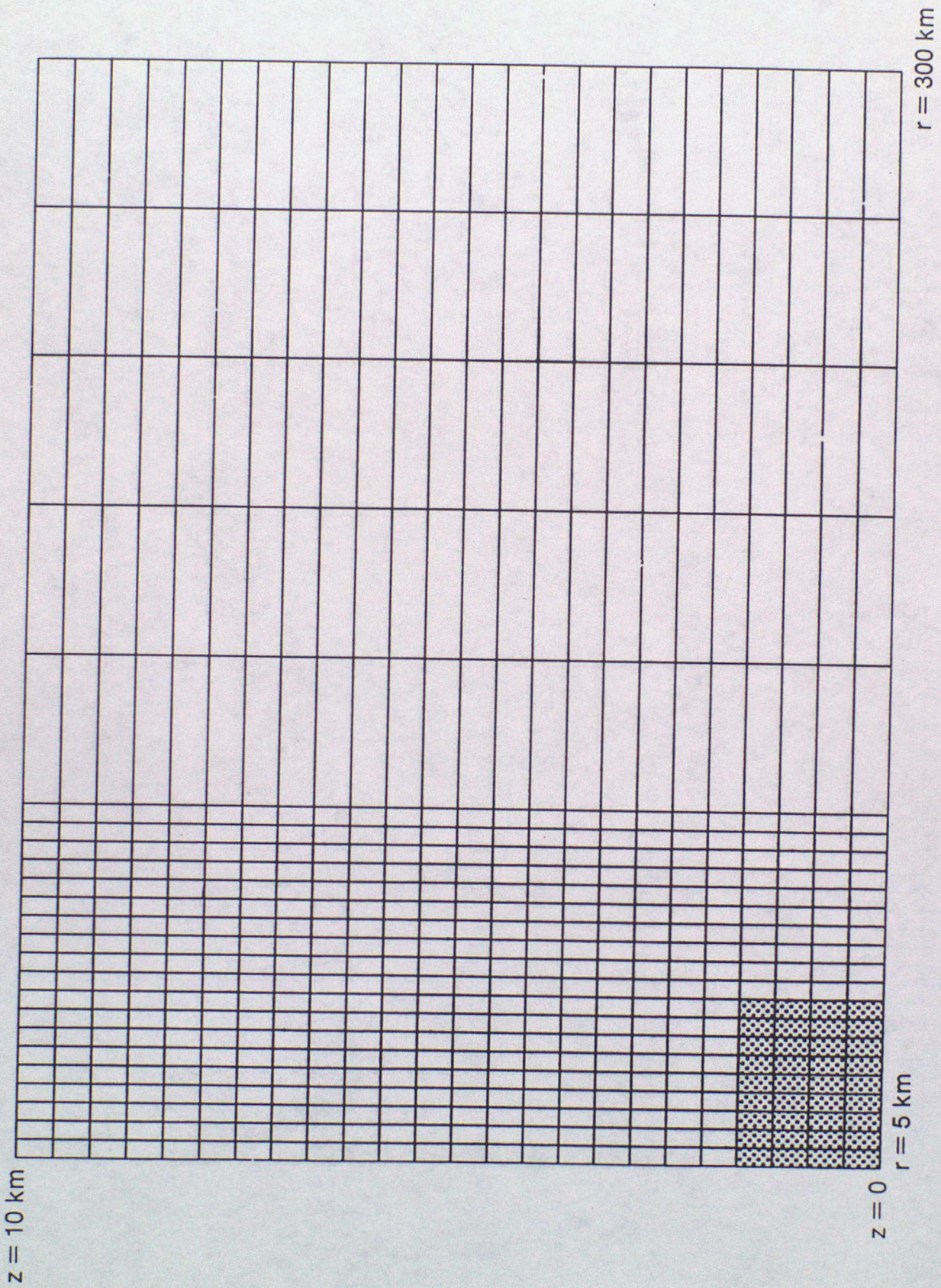

Fig. 2(c)

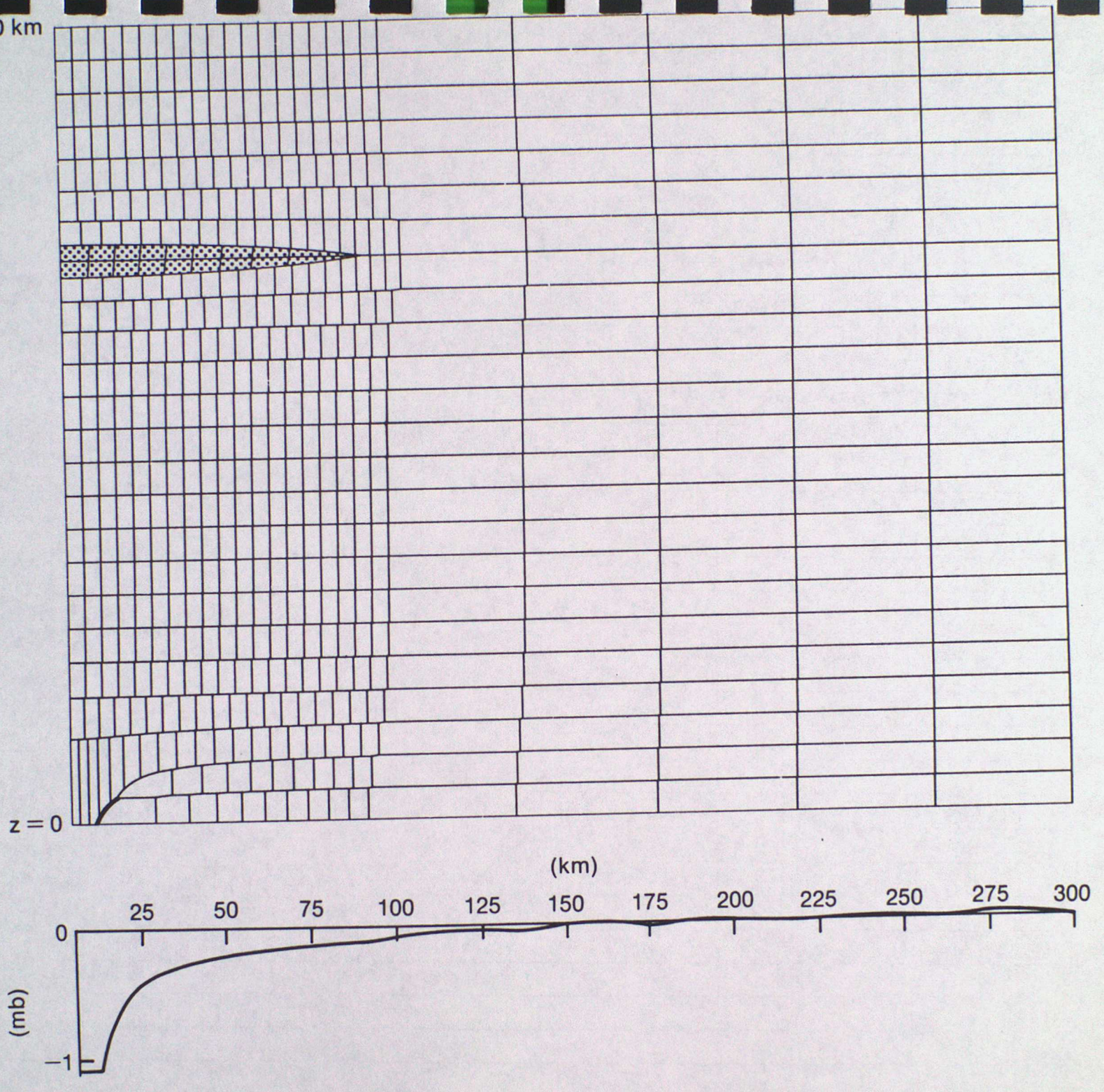

Fig. 3(a)

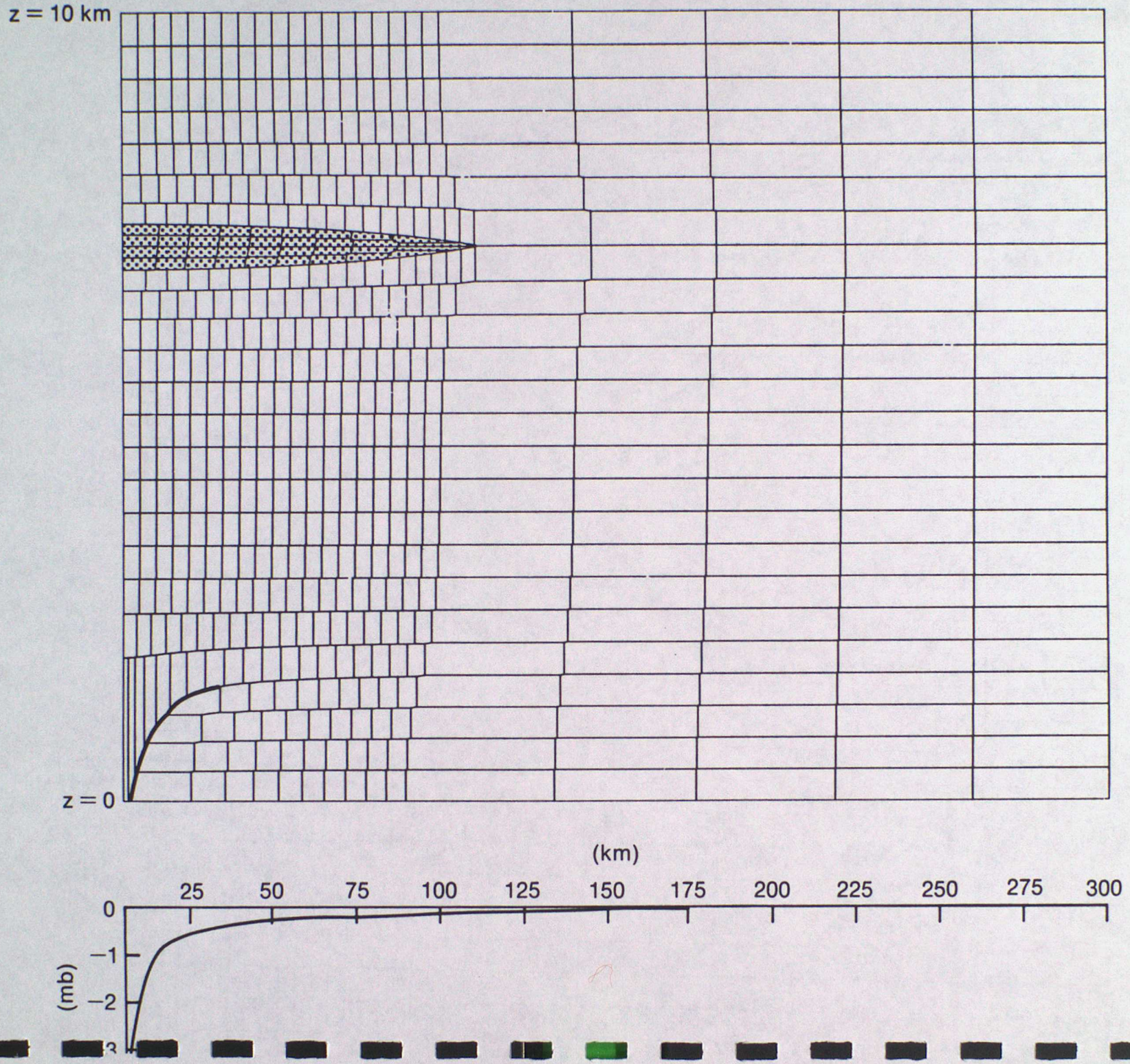

Fig. 3(a)

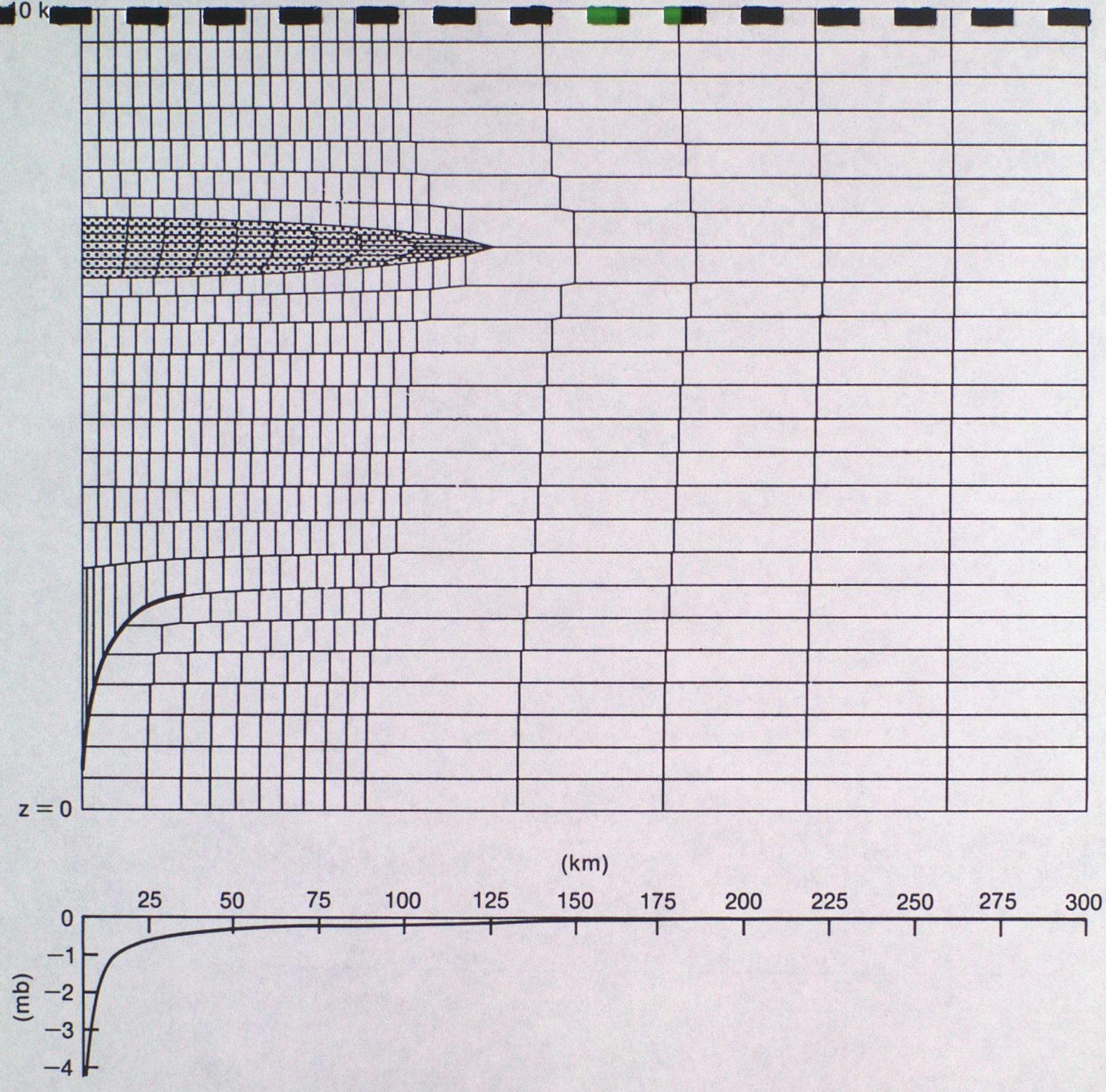

Fig. 3 (c)

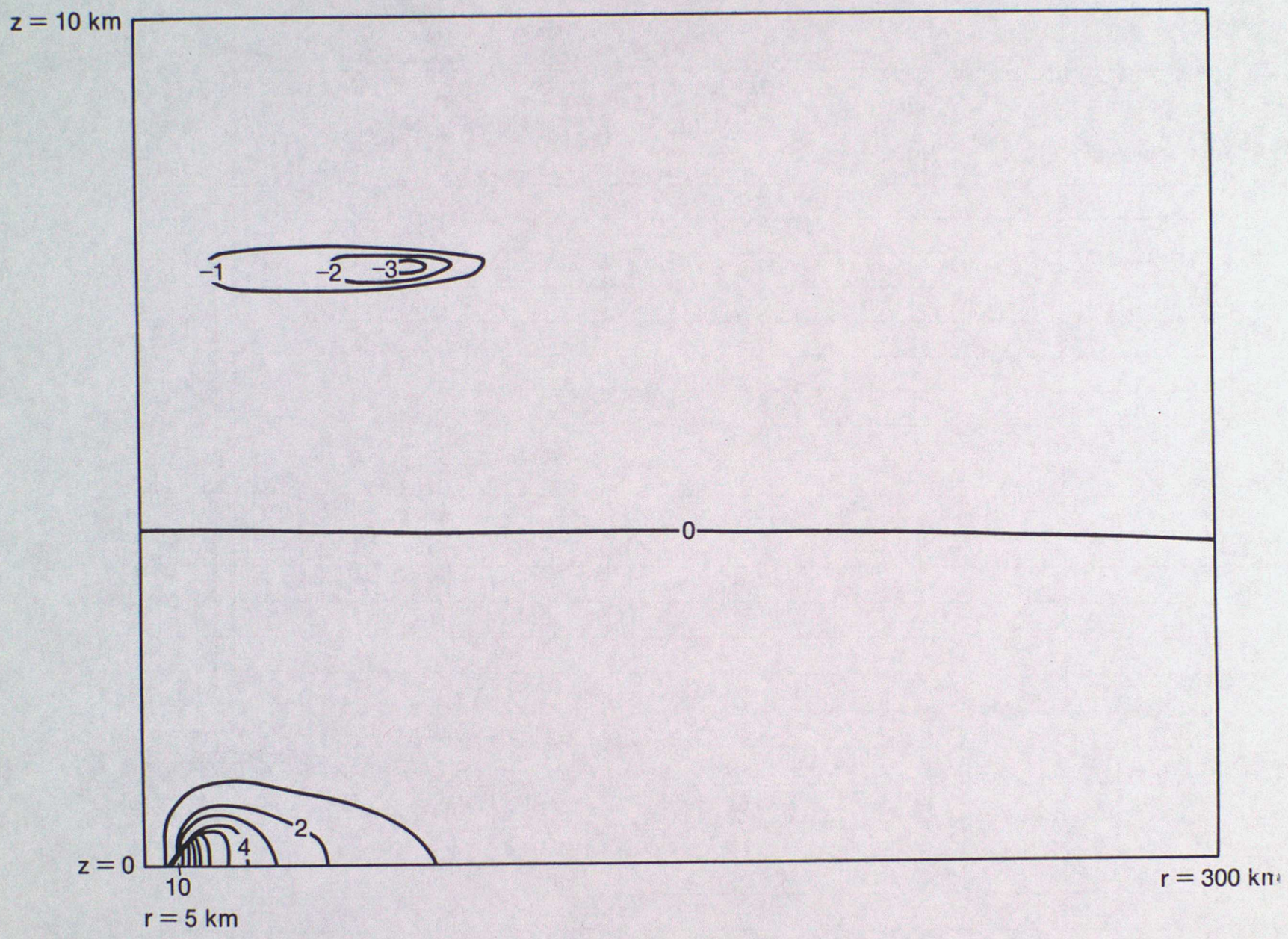

Fig. 4 (a)

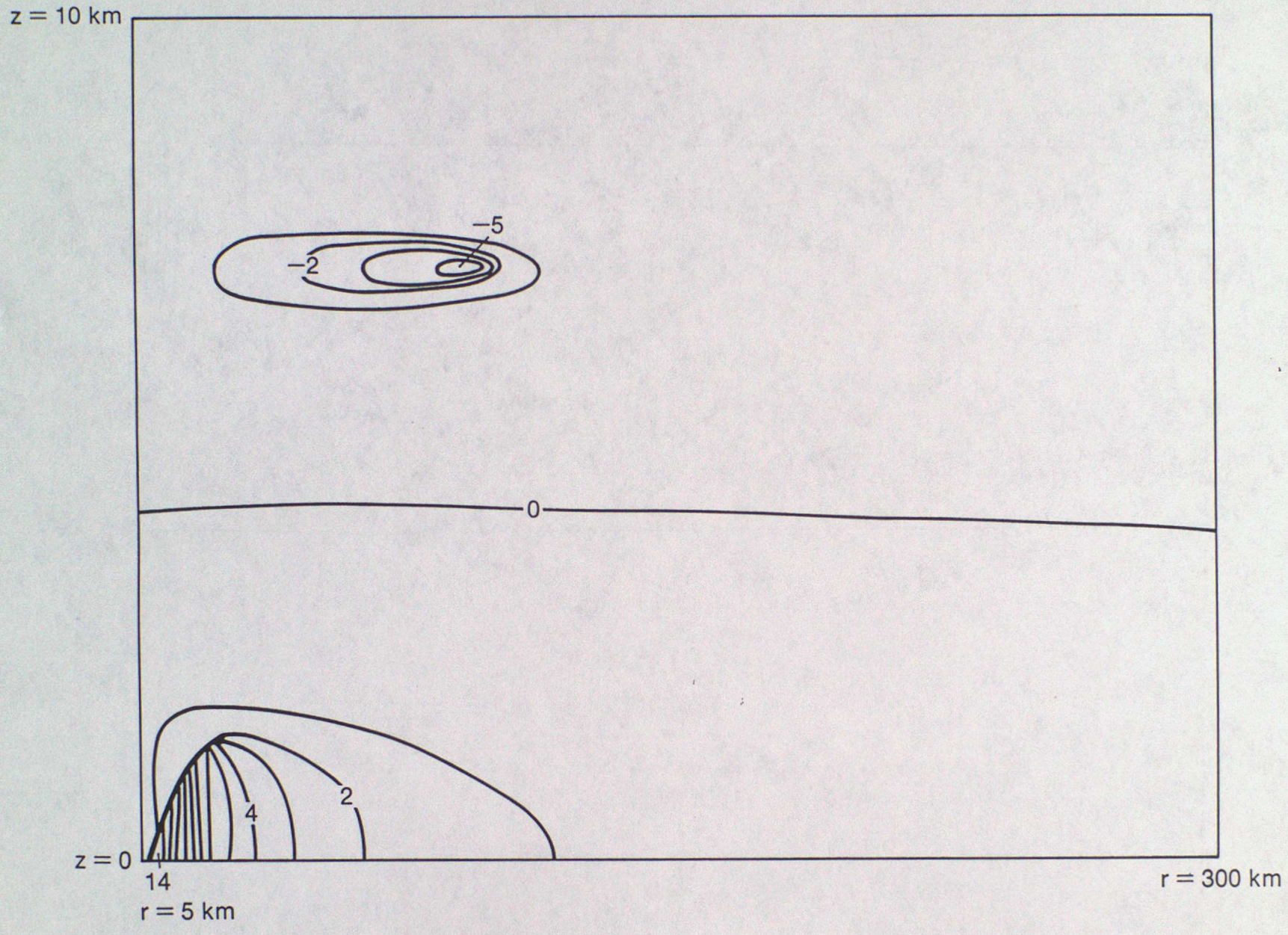

Fig. 4(b)

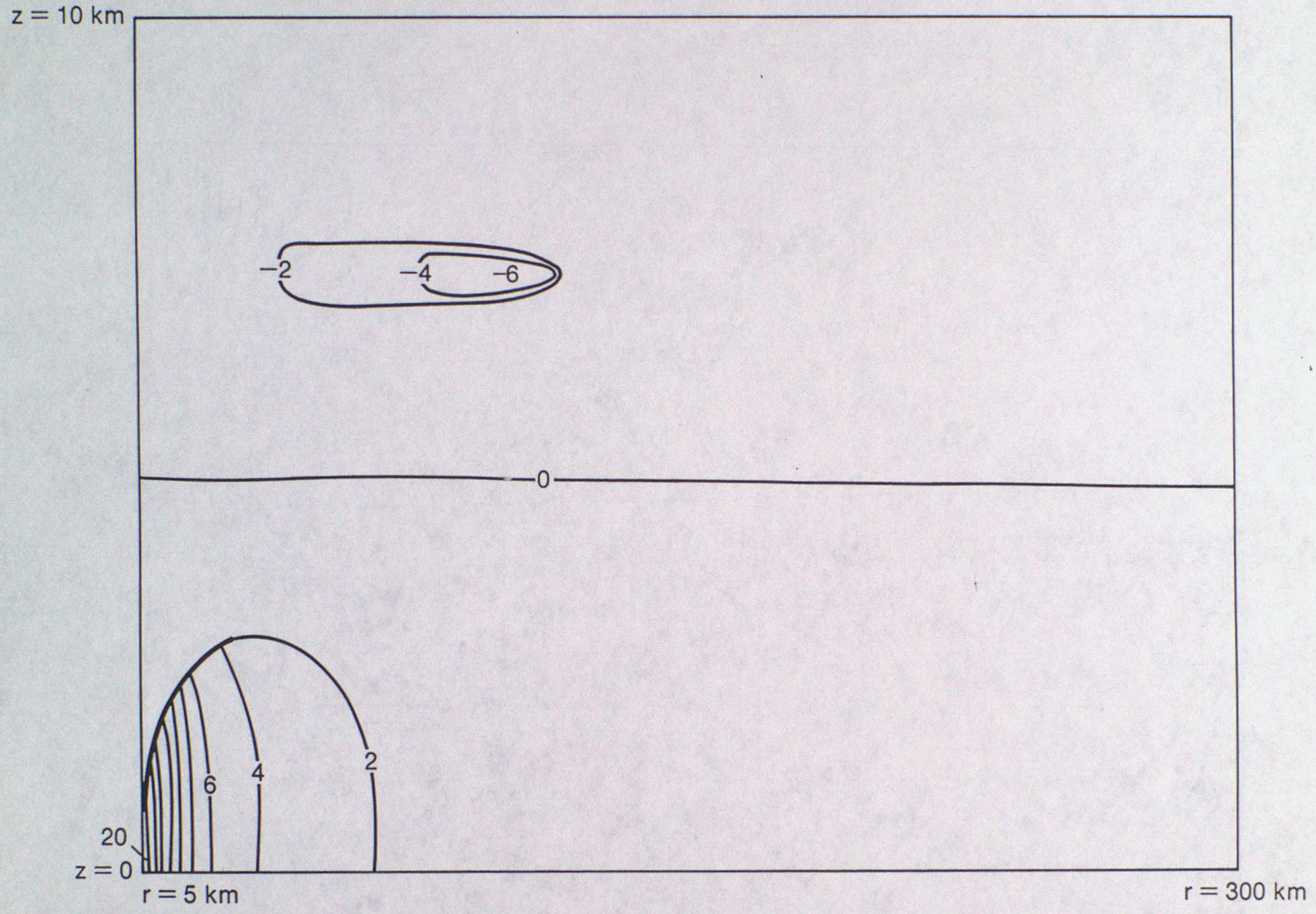

Fig. 4 (c)

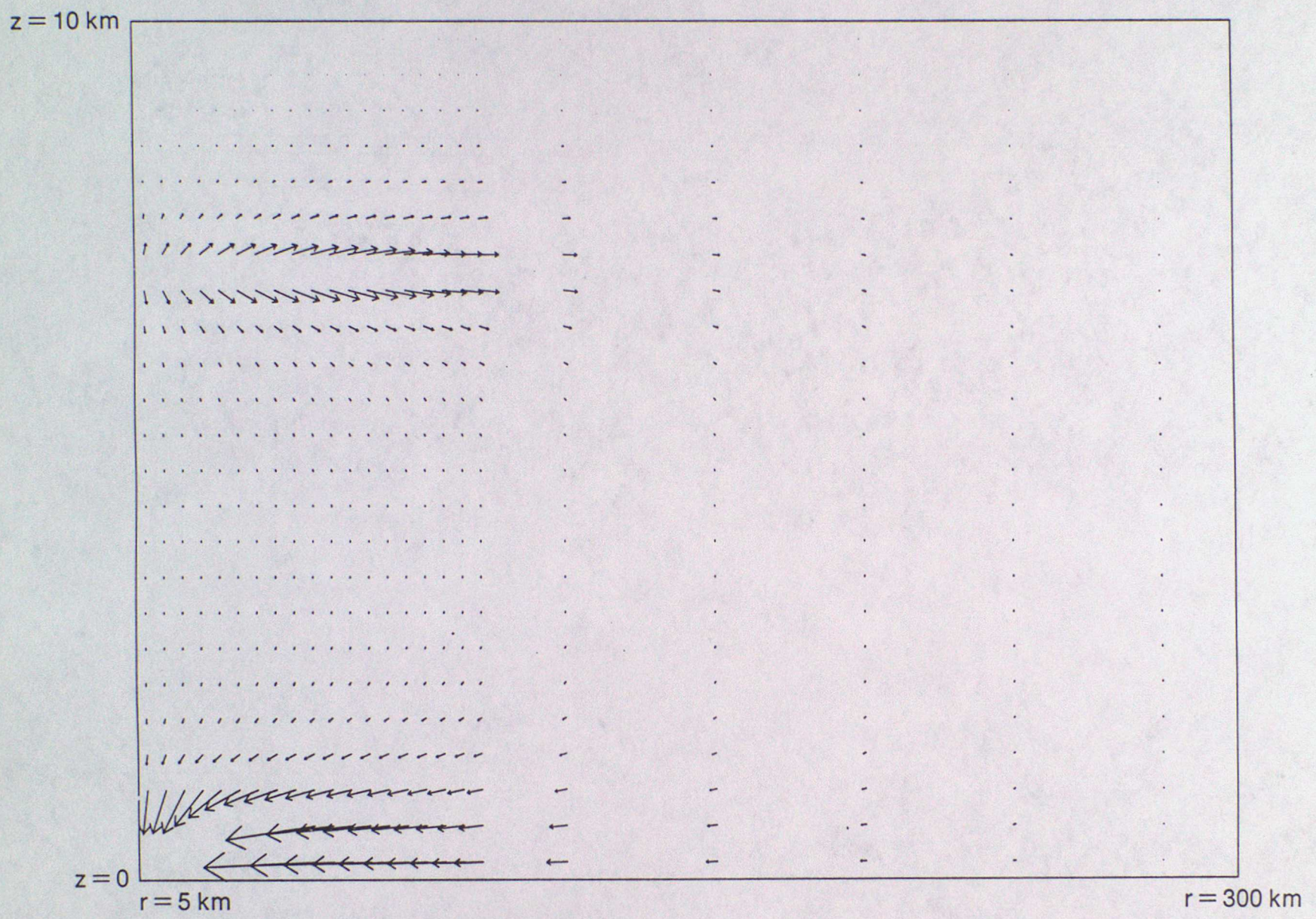

Fig. 5 (a)

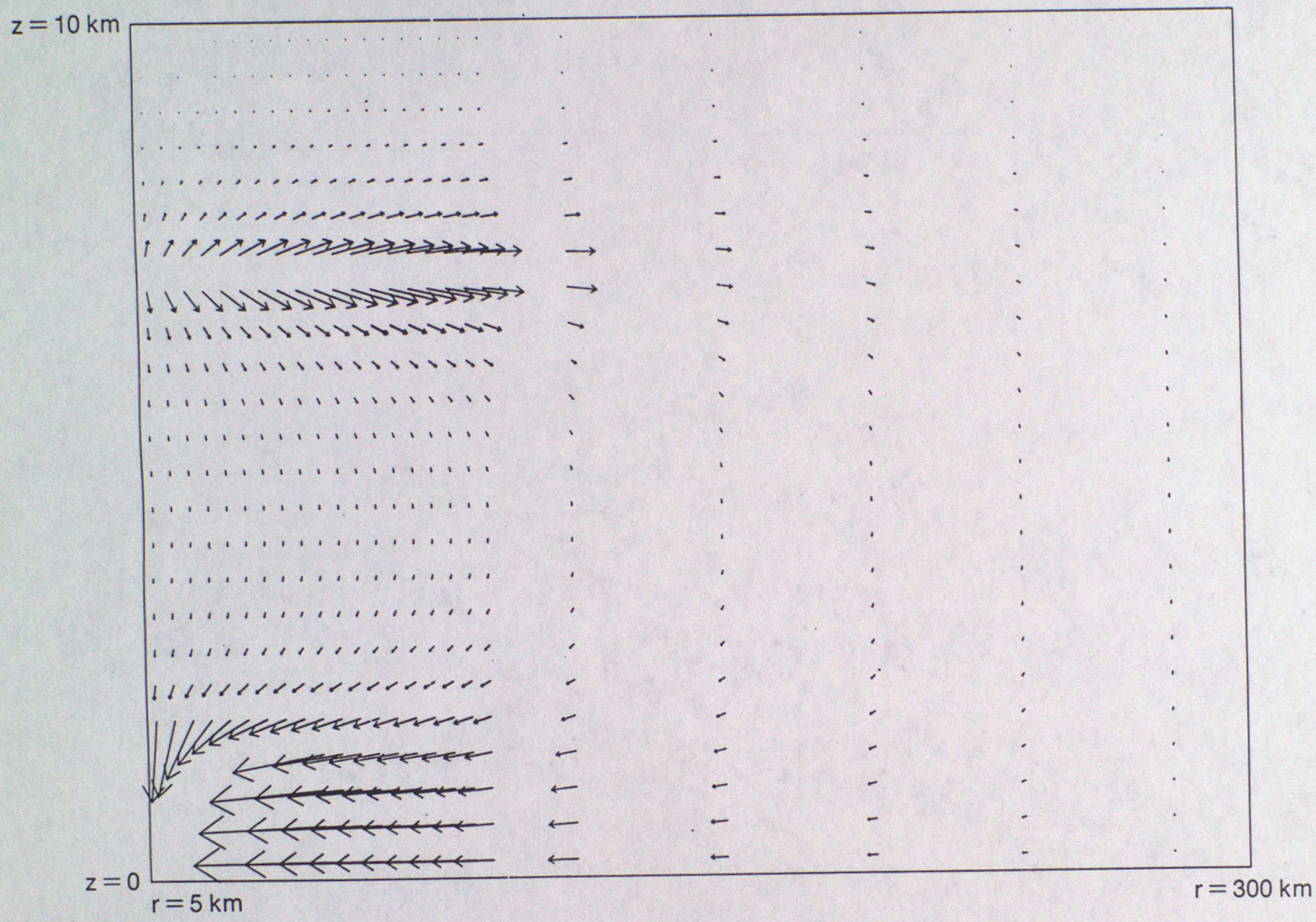

Fig. 5 (b)

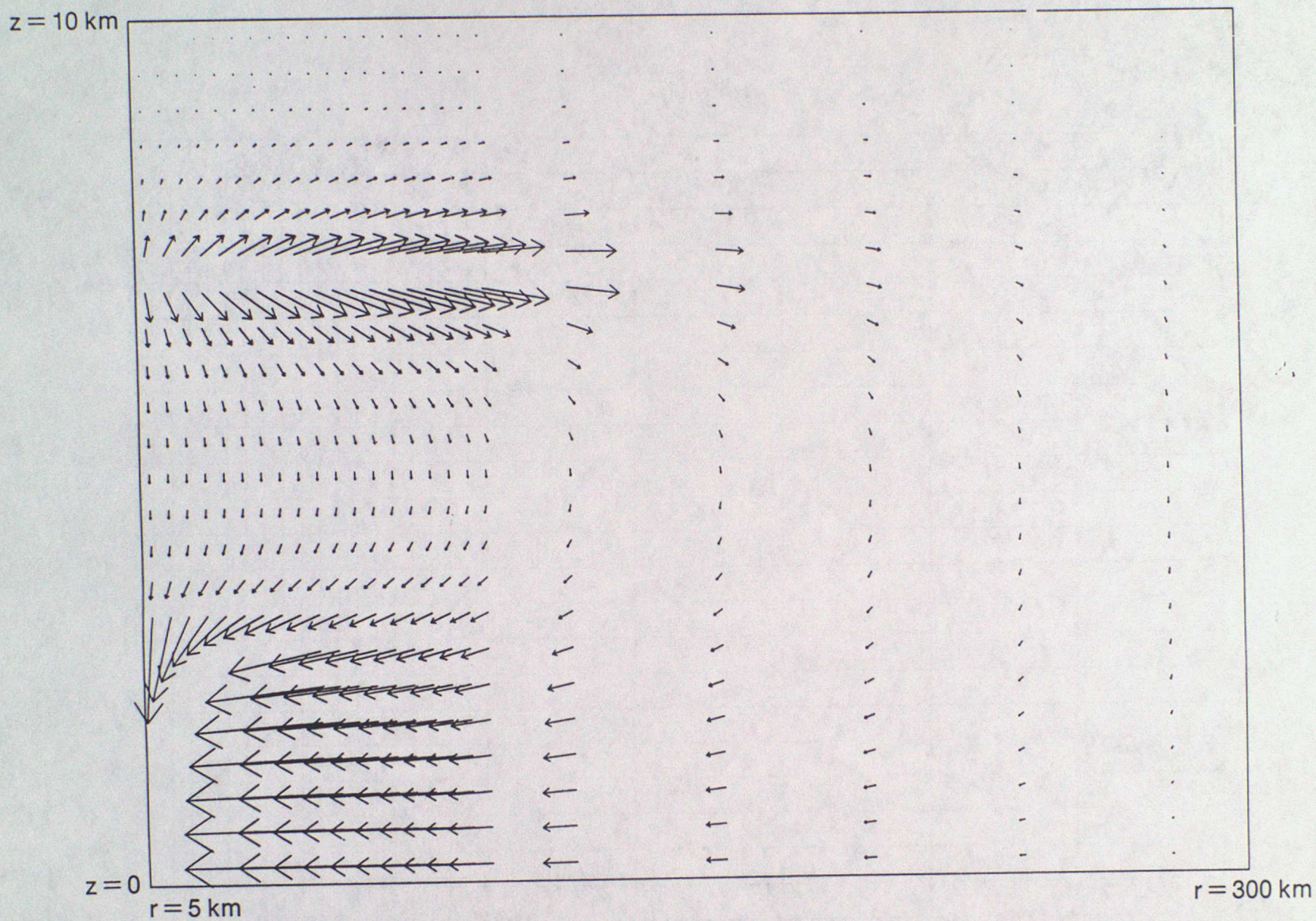

Fig. 5(c)

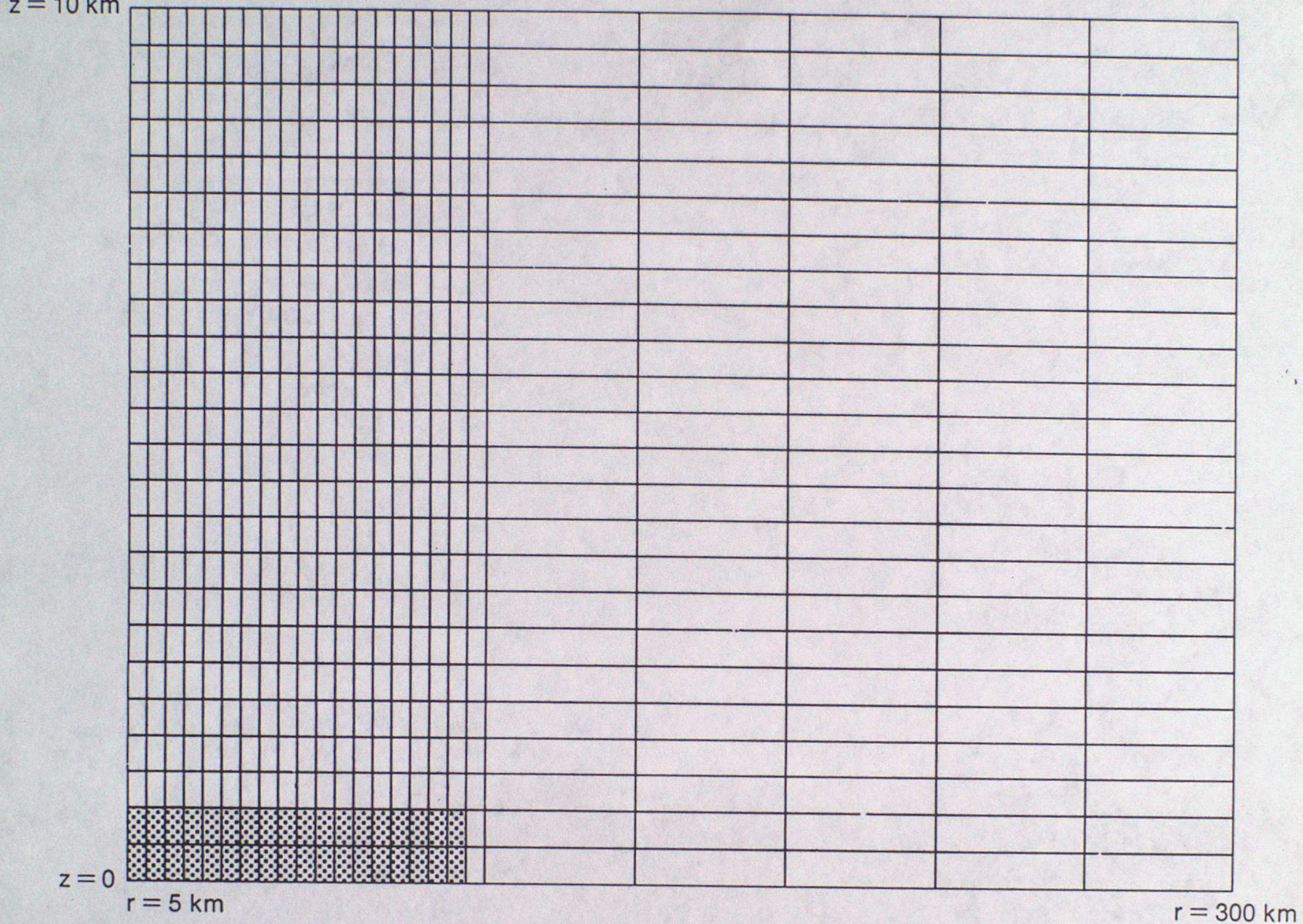

Fig 6(a)

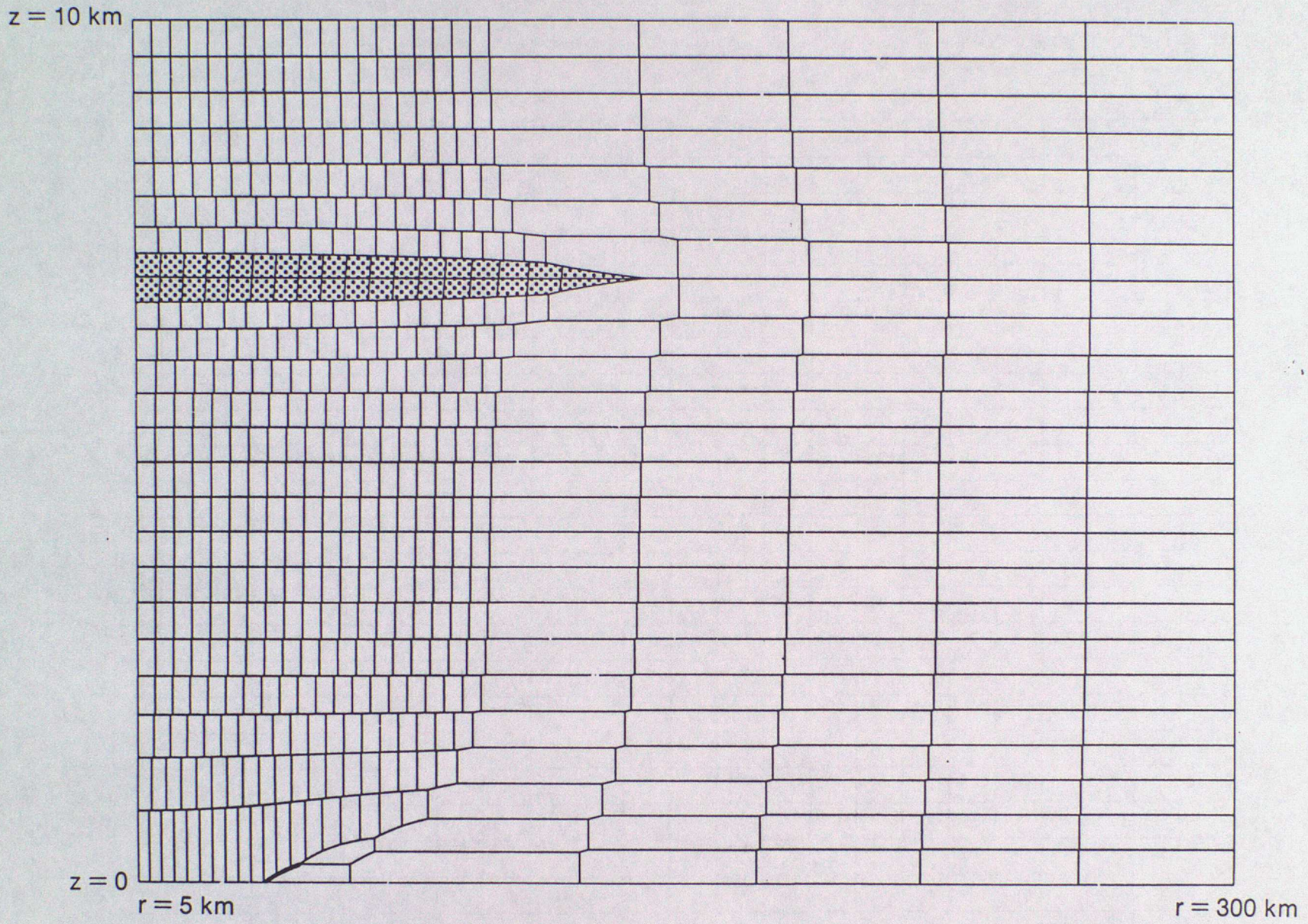

Fig. 6 (a)

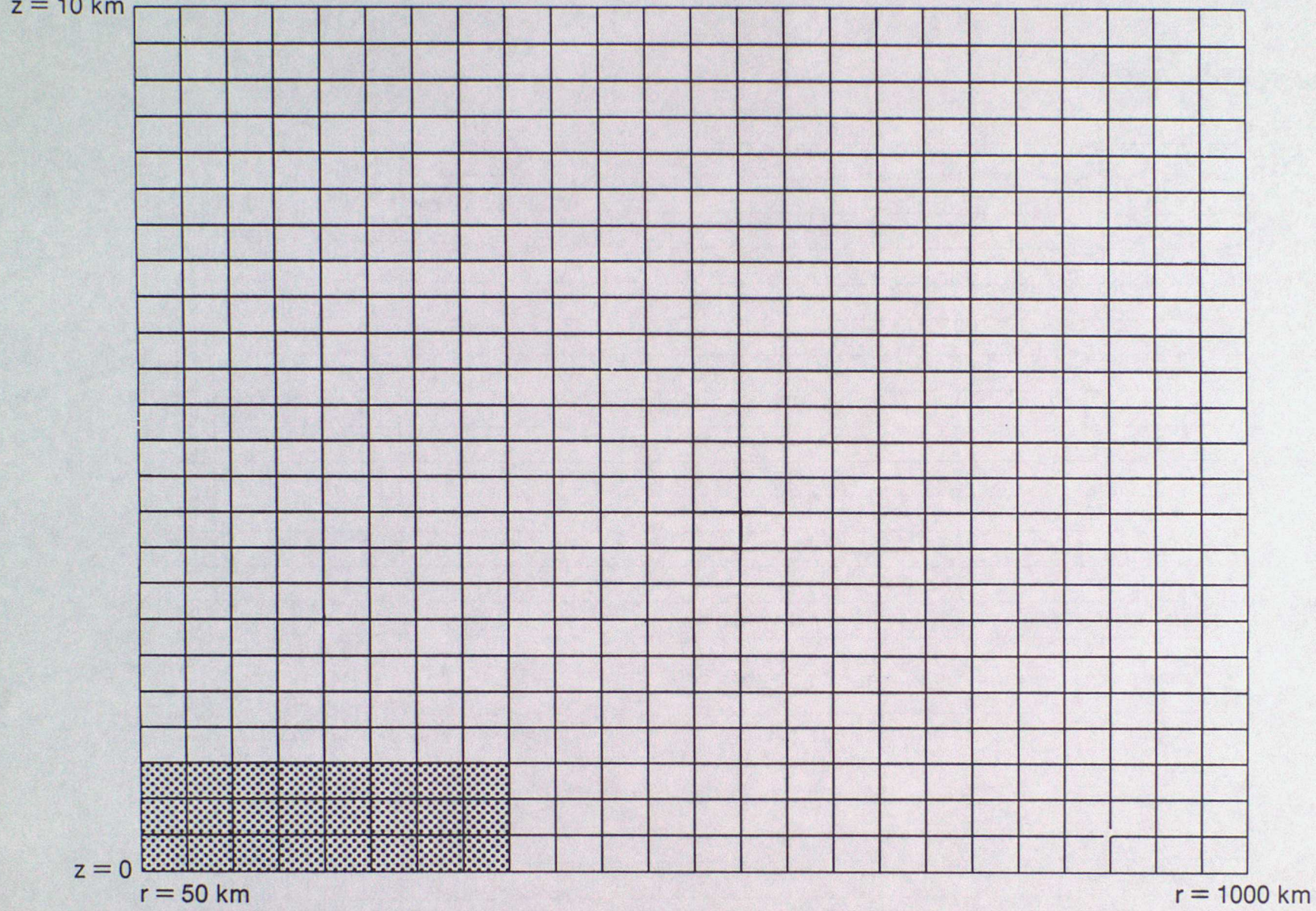

Fig. 7(a)

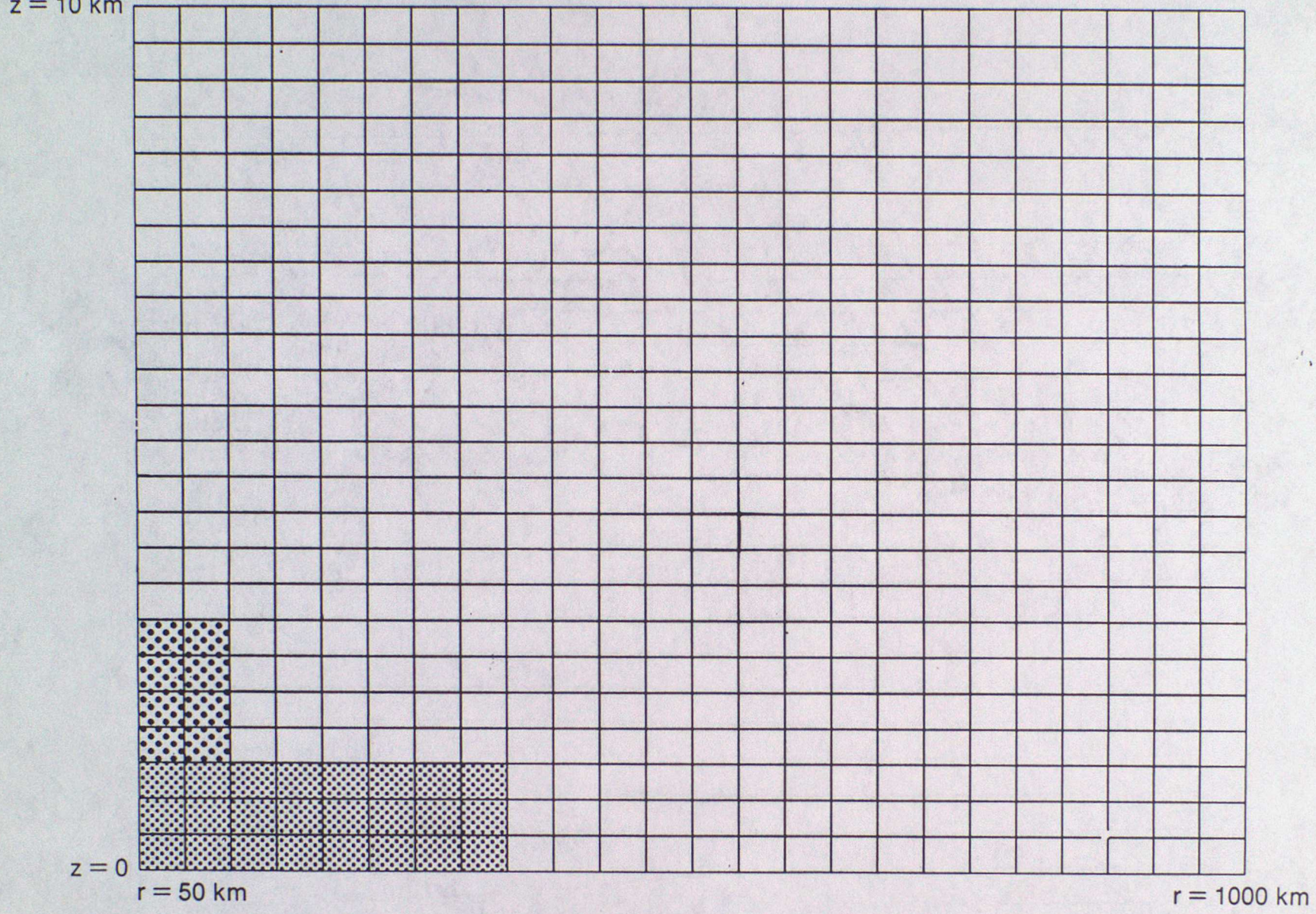

Fig. 7(b)

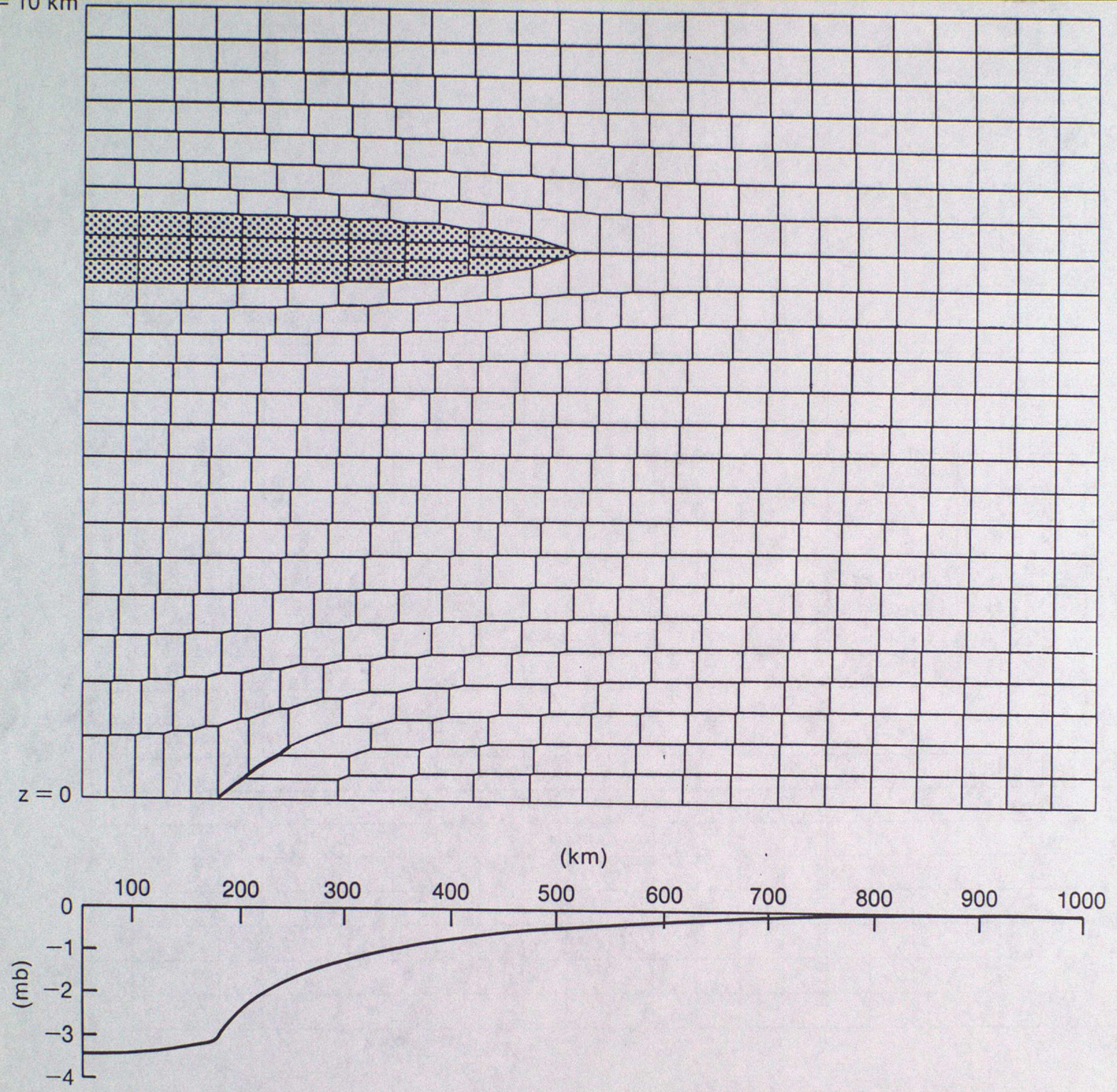

Fig. 8 (a)

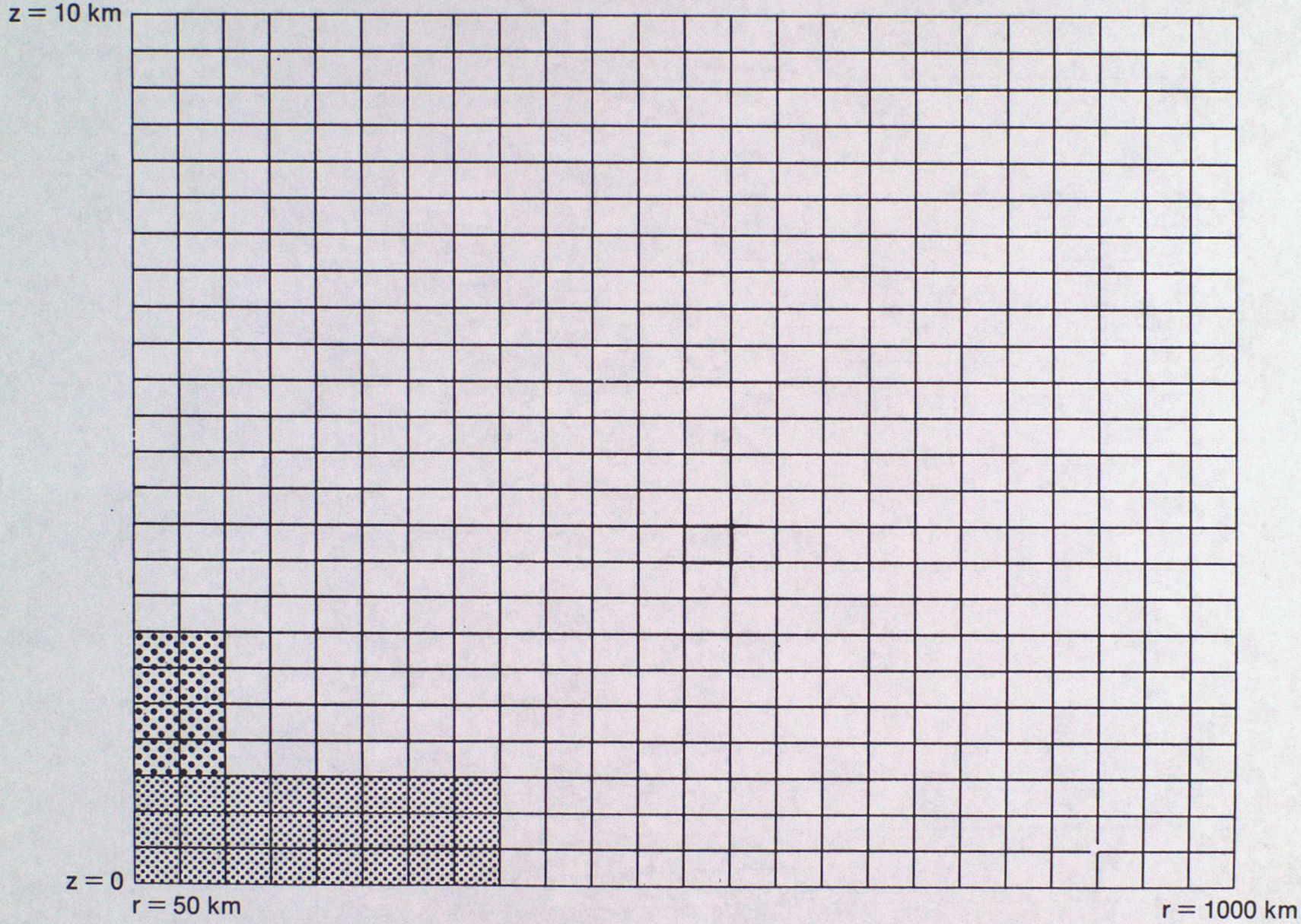

Fig. 7(b)

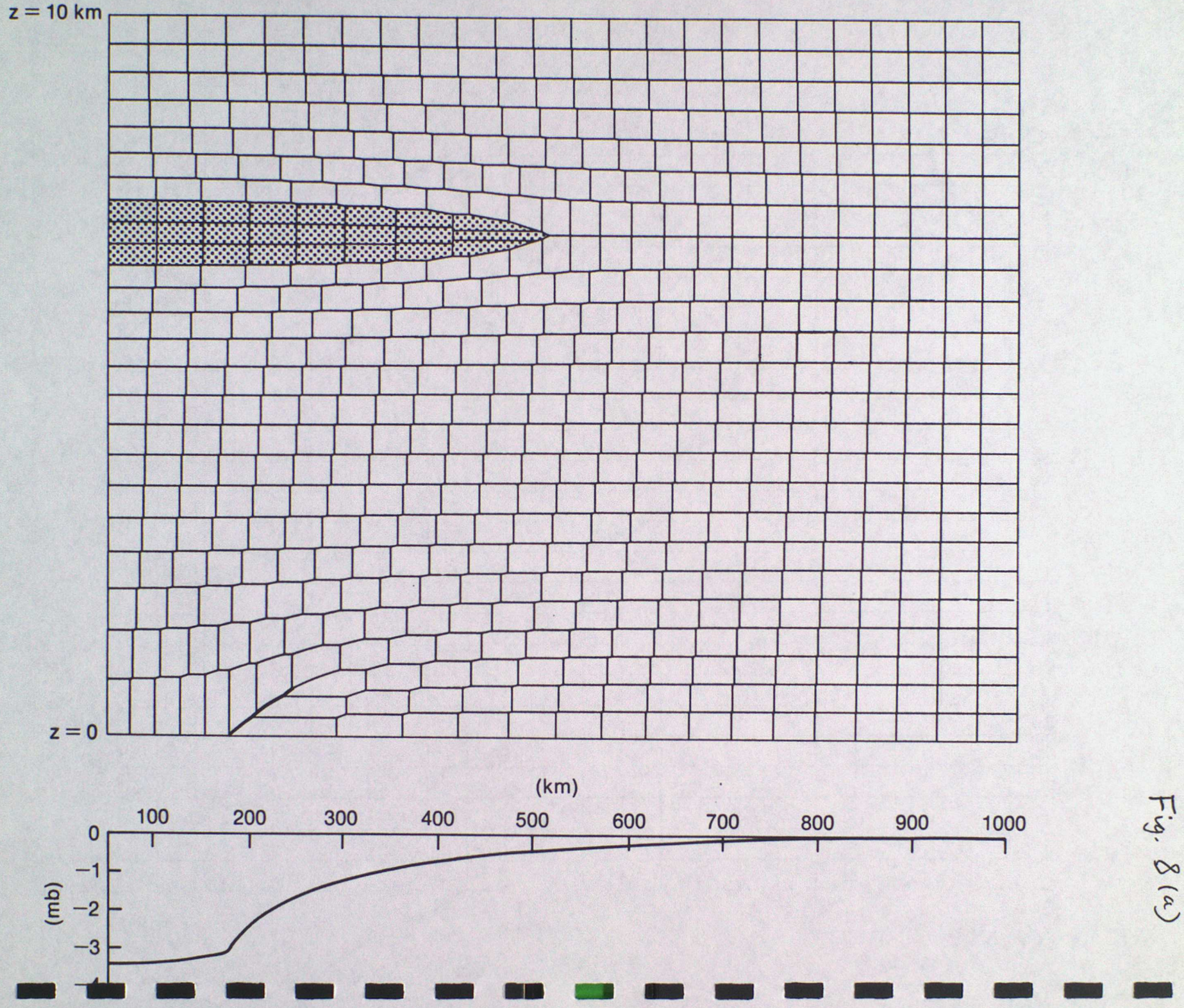

Fig. 8 (a)

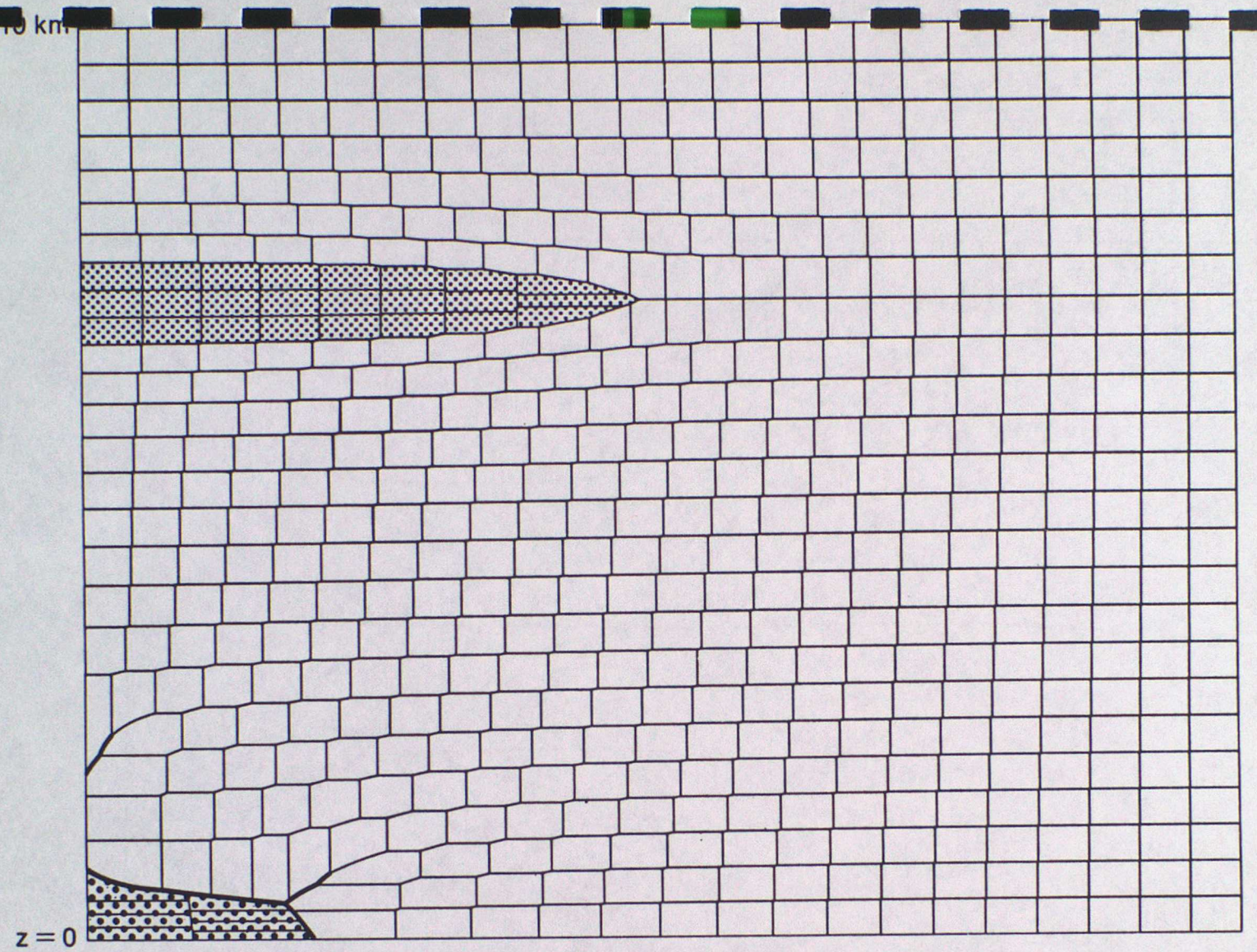

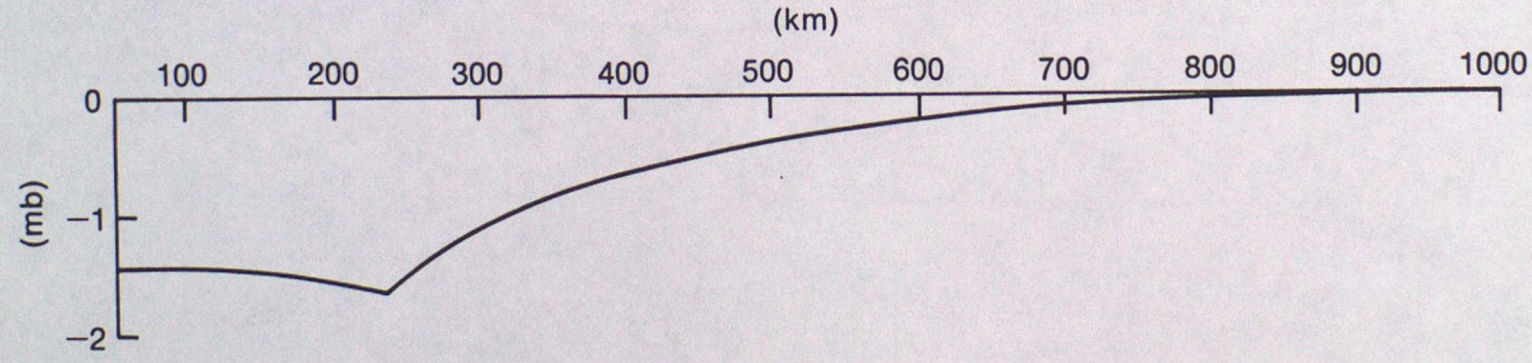

Fig. 8(b)

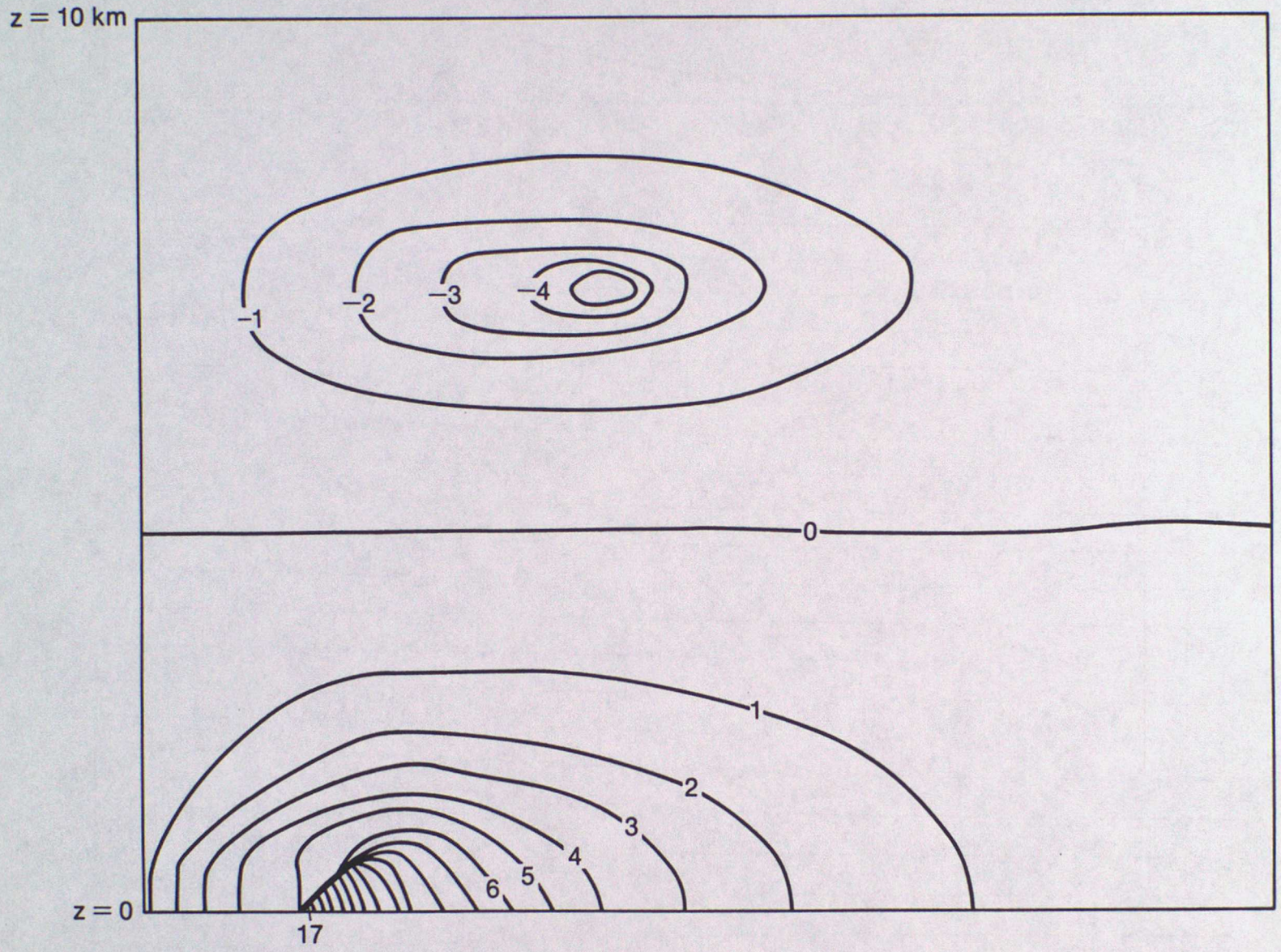

Fig. 9(a)

Fig. 9(b)

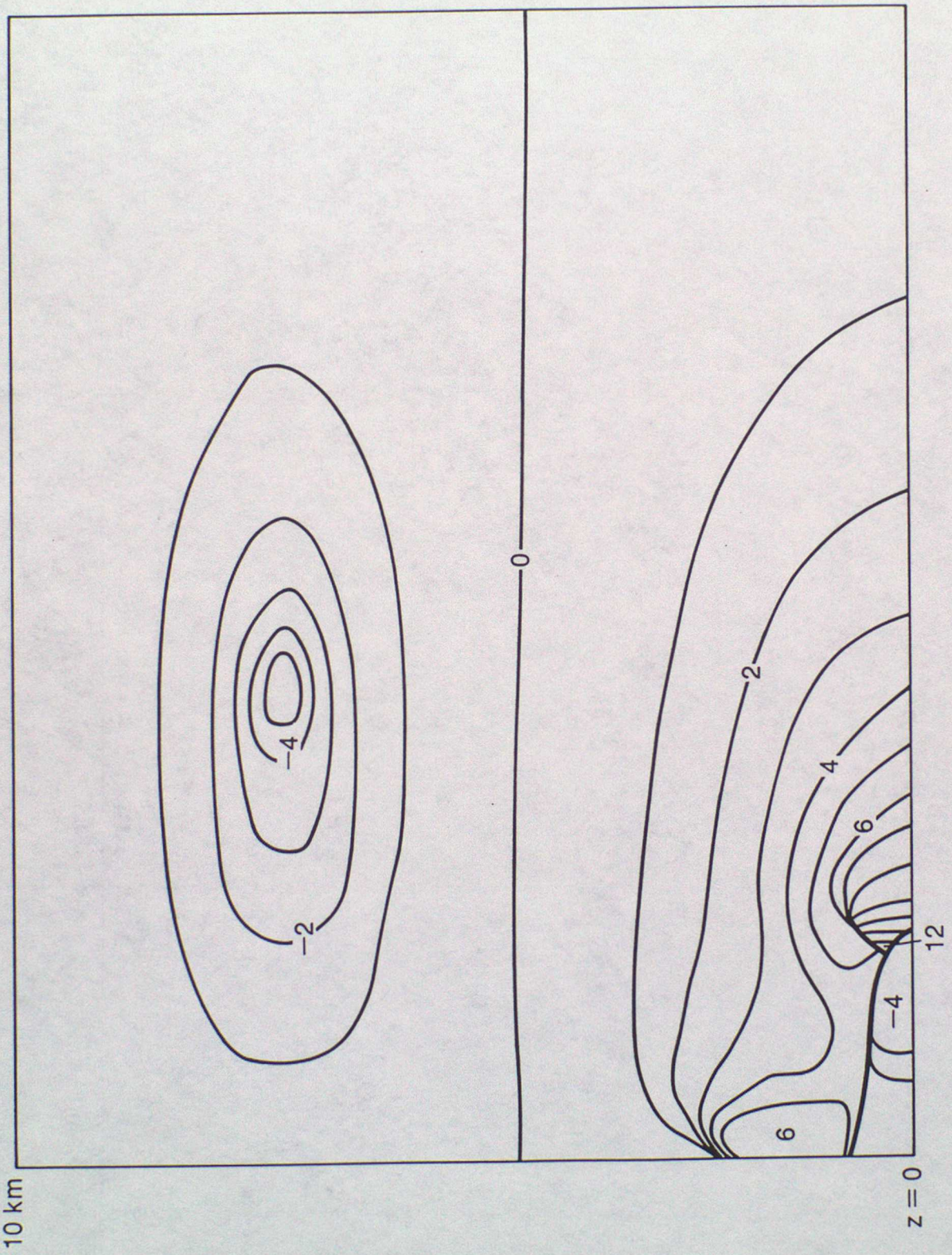

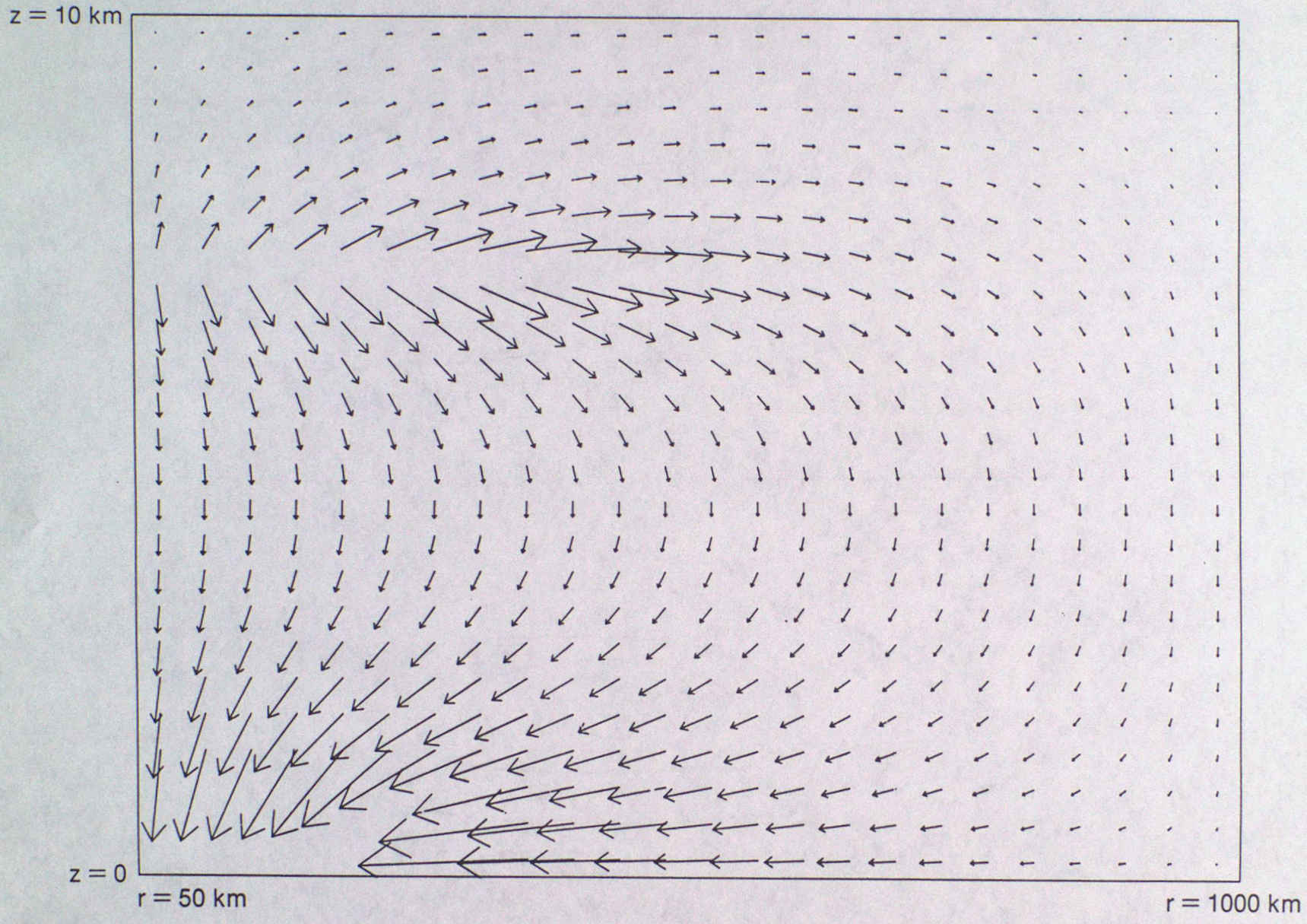

Fig. 10(a)

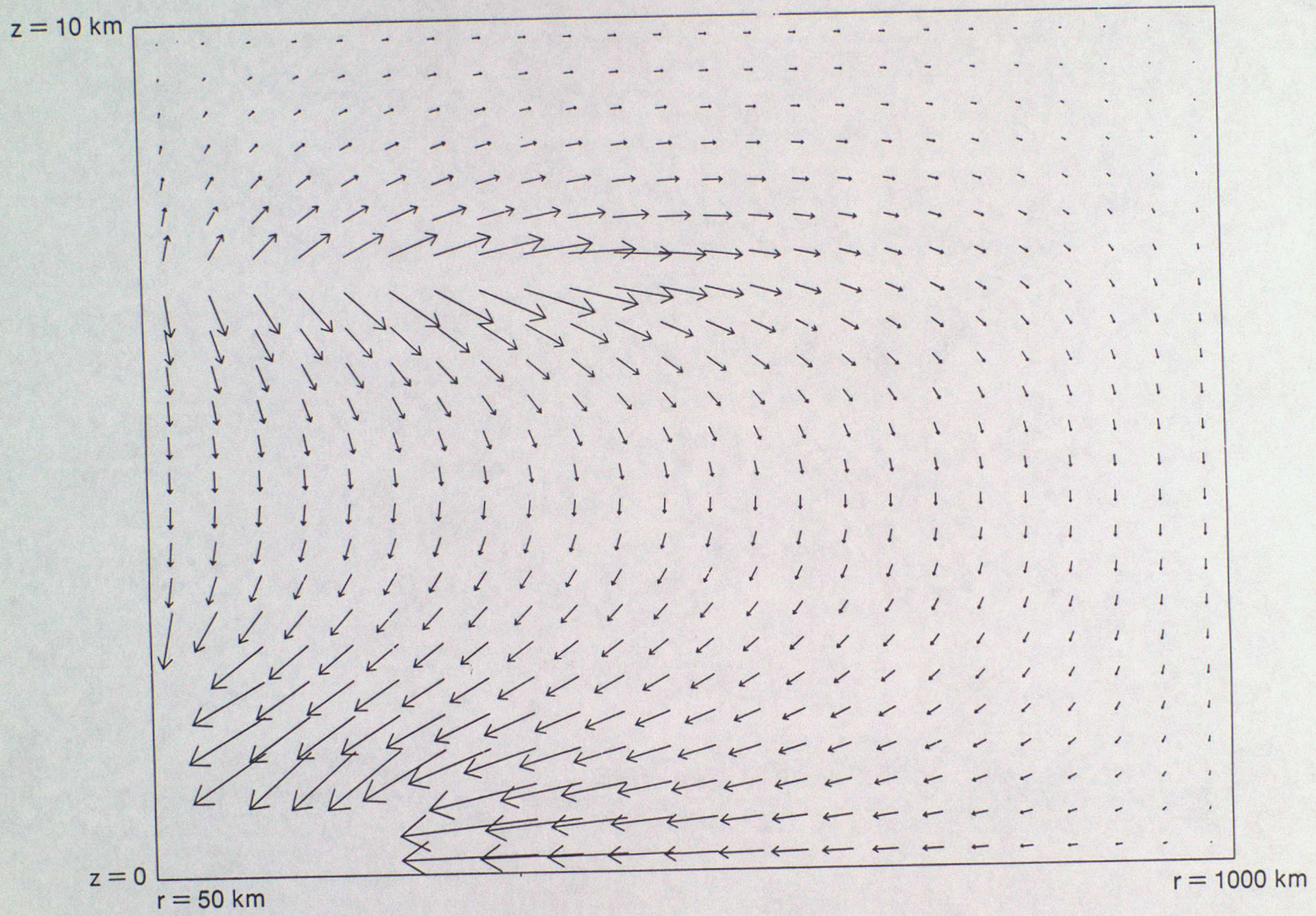

Fig. 10(b)

Fig. 11